Supplemental Material

Water Greatly Impacts on the Nanomechanical Degradation of Functionalized Surfaces

Martin E. Zoloff Michoff,* Przemysław Dopieralski,† and Dominik Marx

Lehrstuhl für Theoretische Chemie, Ruhr–Universität Bochum, 44780 Bochum, Germany

---

* martin.zoloff@theochem.rub.de; Permanent Address: INFIQC–CONICET, Departamento de Química Teórica y Computacional, Facultad de Ciencias Químicas, Univesidad Nacional de Córdoba, Córdoba, Argentina

† Permanent Address: Faculty of Chemistry, University of Wroclaw, Joliot–Curie 14, 50-383 Wroclaw, Poland

CONTENTS

I. MODELING THE PEG–TA MOLECULE

As a first step, the polyethylene glycol (PEG) molecule functionalized by adding a thioctic acid (TA) anchor yielding PEG–TA has been devised. To this end, we studied three PEG chains of different length depicted in Fig. S1, and probed their structural responses within PEG–TA to mechanical stretching, which is established by adding a constant tensile force as visualized by arrows shown in that figure. These calculations were carried out using the Gaussian 09 [1] program package together with using our in–house implementation to add constant external forces; the unrestricted BLYP density functional together with 6-31G* basis set has been used for these explorative calculations. The three PEG–TA molecules were first optimized in the absence of external force and, subsequently, the magnitude of the force, F, was increased in 0.5 nN increments up to 5 nN, while optimizing the PEG–TA structure subject to a given force at each elongation. This allows us to analyze the structural distortion effects due to purely mechanical stretching on the PEG–TA molecule itself.

The largest PEG–TA molecule consists of two ethylene glycol units attached to TA (dubbed LONG), see upper–right panel of Fig. S1 for its structure. In direct comparison to this reference, we have investigated the mechanical properties of two shorter models, one using a modified version the thioctic acid with two CH_2 units less (SHORT-1) and another with with one ethylene glycol unit less (SHORT-2). Then the evolution of selected structural parameters as a function of the applied tensile force for the three molecular models is shown in Fig. S1. These parameters are the relative stretching coordinate, q, defined as the distance between the atoms to which the constant force F is applied with respect to that distance in the absence of force $F = 0$, the $C(H_2)$–O–$C(H_3)$ bond angle the between the last three heavy atoms in each PEG–TA model.

As can be observed from Fig. S1, the prominent characteristics displayed by these important structural parameters as a function of force in the largest model, LONG, are close to quantitatively retained in the smallest model, SHORT-2. Therefore, SHORT-2 is the molecular model chosen to represent the PEG-TA molecule in our full ab initio molecular dynamics (AIMD) [2] simulations that allows us to investigate at a sufficient level of sampling statistics (i.e. trajectory length) purely mechanical as well as mechanochemical degradation phenomena of the total gold/molecule/water system that is visualized in Fig. 1 of the main text (wherein the abbreviation PEG-TA exclusively refers to the present SHORT-2 model).

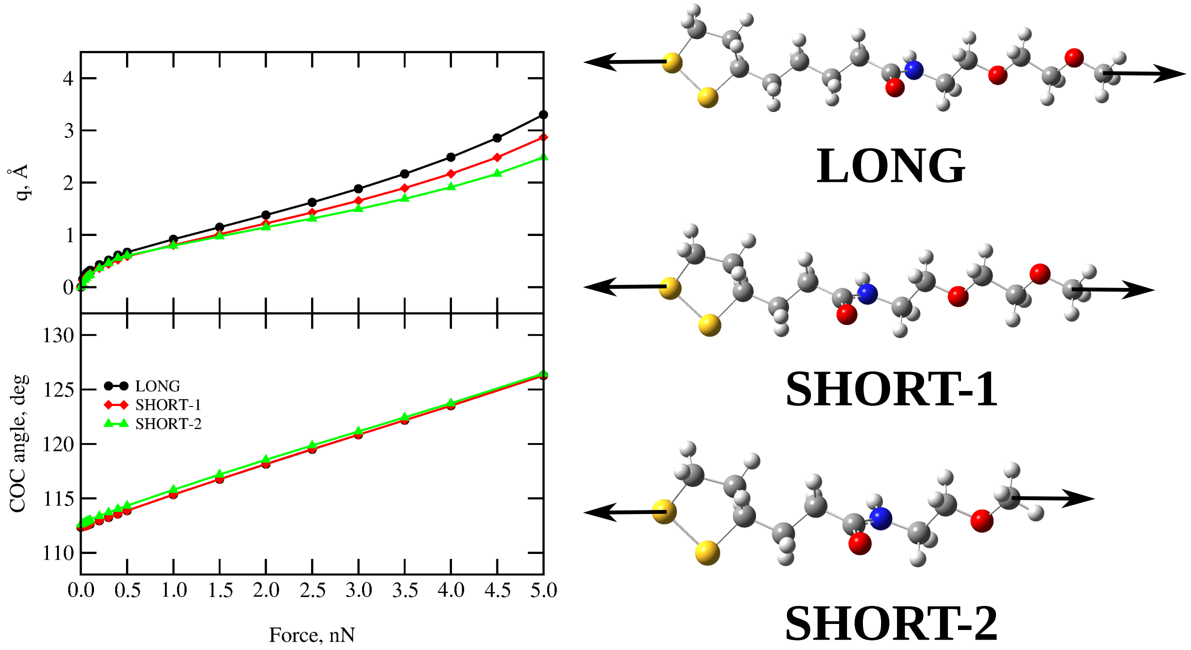

FIG. S1. **Structural properties of the three molecular models LONG, SHORT-1 and SHORT-2 (see text) of the PEG thioctic acid molecule (PEG–TA) as a function of the external force applied** F. Left panels from top to bottom: Relative stretching coordinate q (see text) and $C(H_2)$–O–$C(H_3)$ angle. The molecular structures of the three PEG–TA models are illustrated in the corresponding right panels where the arrows indicate the atoms on which the constant tensile force is applied.

II. MODELING THE PEGYLATED AU(111) INTERFACE AND MECHANICAL STRETCHING IN VACUUM

As mentioned in the main text (where additional computational details not repeated here can be found), our Au(111) surface model consists of a 5×6 slab of 4 gold layers with one additional Au adatom placed at a hollow site as depicted in Fig. 1 of the main text. Here, it is worth to mention that using a four-layer gold slab interfaced with liquid water has recently been validated by explicit convergence tests with reference to the use of six layers [3]. In addition, we have monitored whether the lattice structure of the two middle gold layers, i.e. those between the fixed bottom layer and the top layer that directly interacts with interfacial water and the covalently anchored molecule, is getting distorted during our mechanochemical studies. No such artifacts were observed, thus supporting the aforementioned earlier finding by others that four gold layers are sufficient to describe the bulk metal also in the present case.

On that gold surface, the PEG–TA molecule (namely, SHORT-2 from the previous section) was anchored by means of two S–Au bonds involving the two sulfur atoms of the bidentate thioctic acid terminus, which we label throughout by S(1) and S(2) as defined in Fig. 1 of the main text. In this tweezer-like arrangement, the $\mathrm{Au}^\star$ adatom is located in between these two S atoms which form the S(1)–$\mathrm{Au}^\star$ and S(2)–$\mathrm{Au}^\star$ covalent bonds as visualized by the structure depicted in Fig. 2a of the main text.

This particular bonding motif was chosen in such a way as to resemble the S–Au–S pattern exhibited by thiole–based SAMs on Au(111) surfaces at low coverage in the stripe phase [4], see Figure 2a and 2b therein (where $\mathrm{Au}^\star$ is denoted as $\mathrm{Au_a}$ in blue while the S atoms are colored in red). In this case [4], the two sulfur atoms stem from two different but closeby thiolate molecules, whereas in the present case the two S sites are offered by the same bidentate thioctic acid anchor of the PEG–TA molecule. This initial bonding motif gets strongly distorted upon mechanical pulling, see the transformation of structure 1 up to detachment due to isometric stretching in Fig. S2 and isotensional stretching at 1.0 and 1.6 nN in panels b and c of Fig. 2 in the main text (the latter providing our pre-stretched configuration for subsequent AIMD simulations, see below). Importantly, the two vastly different stretching techniques applied to the same hybrid metal–organic junction are both found to consistently pull a second Au atom out of the surface (see structure 2 in Fig. S2 and the structure at 1.6 nN in Fig. 2c of the main text), which will play an important role in nanomechanical detachment scenarios as presented in the main text. The Quantum Espresso software [5] (PWscf version 4.1) was used for these optimizations in the absence of solvation water. The PBE [6] density functional and Vanderbildt's ultrasoft pseudopotentials [7] were employed. A plane wave (electronic density) cutoff of 25 Ry (100 Ry) was employed throughout using the Γ–point approximation. This particular electronic structure setup has been carefully validated in previous work [8, 9] for very similar hybrid metal–organic interfaces in vacuum.

The fully optimized PEG–TA/Au(111) system thus obtained in vacuum was used as the initial structure for two types of preliminary static pulling computations, namely at one at constant distance (isometric stretching) and another at constant force (isotensional stretching); we refer to a review article for background and discussion of these complementary methods [10]. In the isometric approach, the terminal C atom of the PEG–TA molecule was constrained to move in the xy plane parallel to the bottom layer of fixed Au atoms. The distance between these two planes, termed pulling distance (Δz), was increased stepwise by increments of 0.2 Å, and full structure optimization was performed at each stretching step while applying this constraint, thus allowing the terminus of the PEG–TA molecule to freely move in the xy plane at a given stretching distance. In the isotensional approach, a constant external force of magnitude F was applied again to the terminal C atom in the direction perpendicular to the bottom layer of fixed Au atoms (while no other constraints acted on the system). Geometry optimizations with the "*damp*" algorithm of PWscf were performed within that setup.

A. Isometric Approach

The results of the static isometric pulling calculations are summarized in Fig. S2 as a function of Δz. It depicts the optimized pulling pathway of PEG–TA on Au(111) in vacuum with a sequence of elastic transformations and plastic transitions, the latter visualized in terms of configurations 2 to 5, until purely mechanical detachment eventually occurs toward structure 6 after significant stretching of the hybrid metal–organic junction beyond about 8 Å. These stages are evidenced by the evolution of the total energy and the restoring force of the system along the pulling distance shown in the left panel of Fig. S2. The

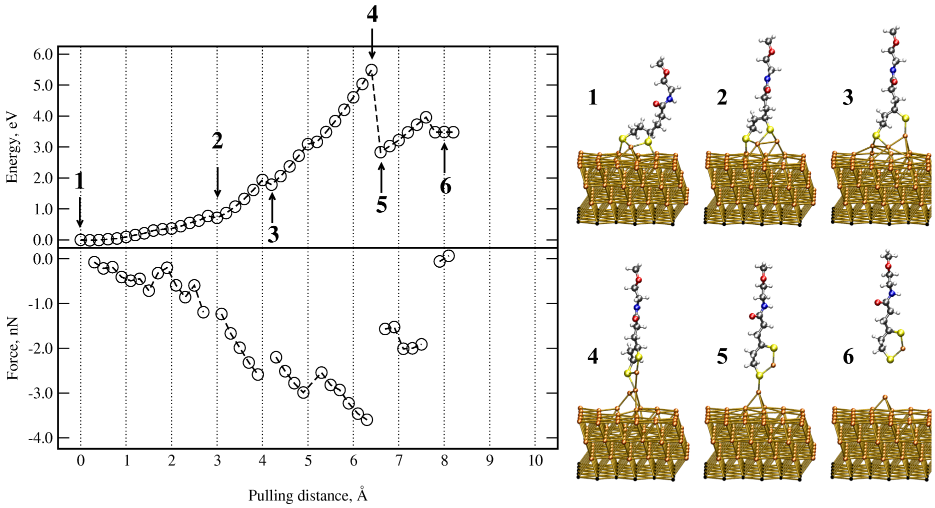

FIG. S2. **Isometric stretching of the PEG–TA/Au(111) surface in vacuum until final purely mechanical detachment**. Left panel: Energy and force profiles as a function of Δz, see text. Right panel: Six relevant structures along the optimized pulling path.

representative configurations along the mechanical desorption pathway in the right panel of that figure illustrate a series of Au–Au and Au–S bond breaking and formation events, with final detachment taking place along with pulling of one Au atom out of the gold surface which finally remains bonded to both S atoms in a tweezer–like arrangement.

The Löwdin population for relevant atoms along the pulling simulation were analyzed and the results are reported in Fig. S3 while the change of selected bond distances along the pulling calculation are compiled in Fig. S4. Notably, the O atom in the –OCH_3 terminal group of PEG–TA becomes more negatively charged, so its proton affinity increases when the molecule is stretched.

This is consistent with what has been observed earlier in the case of the much smaller dimethyl ether molecule [11]. The charge and bond distance variation of the atoms involved in the amide bond suggests that the resonance structure in which the lone pair from the N atoms is donated to the carbonyl carbon, C=O, is destabilized upon mechanical stretching.

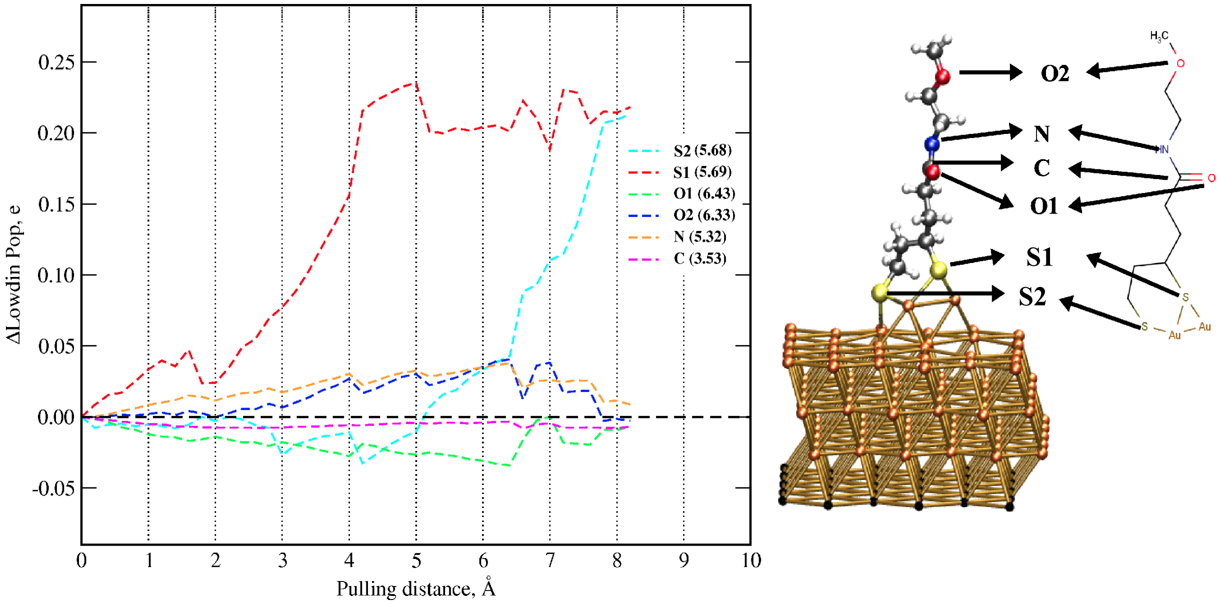

FIG. S3. **Isometric stretching of the PEG–TA/Au(111) surface in vacuum until final purely mechanical detachment.** Left panel: Change of the Löwdin populations (or charges) for important atoms; the initial values at zero pulling are provided in parentheses. Right panel: Labeling of the analyzed atoms in ball–and–stick (left) and schematic (right) representations.

We note that this is in line with previous observations in QM/MM simulations of a peptide under external mechanical stress [12]. The largest variation in Löwdin populations is observed for the sulfur atoms. Notably, in the fist stages of pulling, S(1) being better aligned with the applied force, becomes more negative. At the same time, S(2) becomes slightly more positive initially, but after pulling to 5 Å and beyond also that sulfur atom starts to accumulate negative charge as the force increases.

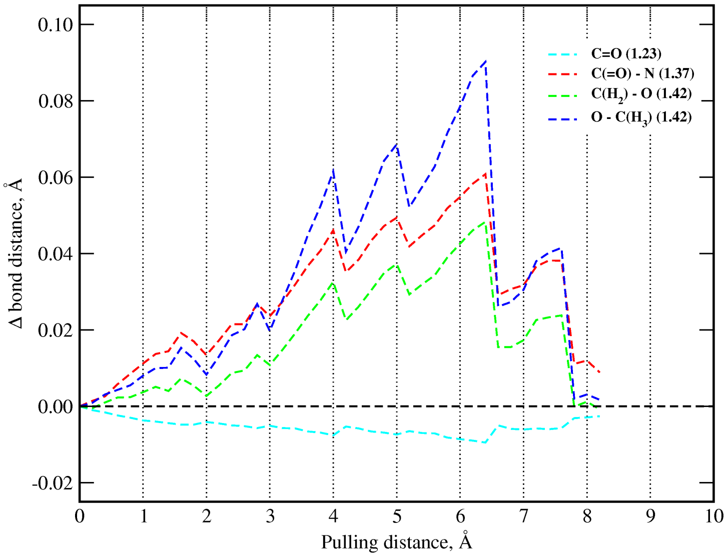

FIG. S4. **Isometric stretching of the PEG–TA/Au(111) surface in vacuum until final purely mechanical detachment**. Change of important bond distances; the initial values at zero pulling are provided in parentheses.

B. Isotensional Approach

Next, starting from the fully optimized PEG–TA/Au(111) structure in vacuum obtained at Δz=0.0 Å, external forces of constant magnitude $F = 1.0$ and 1.6 nN were applied to the terminal carbon atom in the chain. The structure subject to these mechanical forces was again optimized using the "*damp*" algorithm while keeping the bottom layer of Au atoms fixed. The resulting optimized structures at the two different tensile force values are illustrated in Fig. 2 panels b and c of the main text. Most interestingly, the structure obtained at 1.6 nN resembles that from isometric pulling at $\Delta z = 3.0$ Å (compare to configuration 2 in the right panel of Fig. S2). More importantly, in this structure all of the soft intramolecular degrees of freedom, such as dihedral angles, are all fully stretched out. Thus, this pre–stretched structure provides an adequate starting point for our isotensional AIMD simulations, after full solvation with explicit water molecules (see below), in order to study both, purely mechanical and reactive mechanochemical degradation of the metal–organic interface.

C. Assessing System Size Effects

The effect of necessarily having a finite vacuum region normal to the gold surface on the properties of the system studied was evaluated for the extended structure obtained from

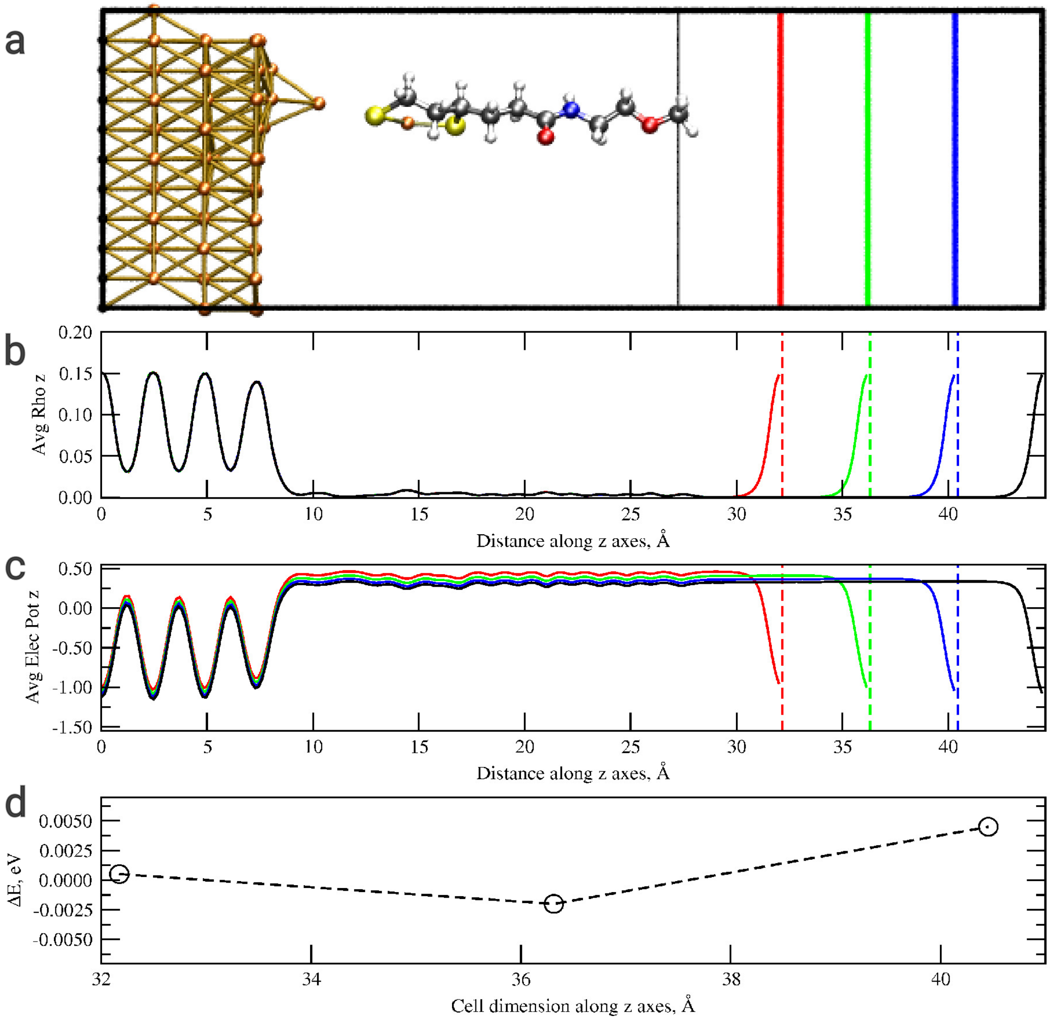

FIG. S5. **Assessing the supercell dimension perpendicular to the gold surface**. From top to bottom: (a) Optimized structure from isometric pulling at Δz=7.6 Å. The different values probed for the supercell dimension in the direction perpendicular to the surface are marked while the largest value of about 45 Å has been used to optimize the depicted structure. (b) Average electronic density in the direction perpendicular to the surface. (c) Average electrostatic potential in the direction perpendicular to the surface. (d) Difference in total energy with respect to the largest value for the supercell dimension in the direction perpendicular to the surface.

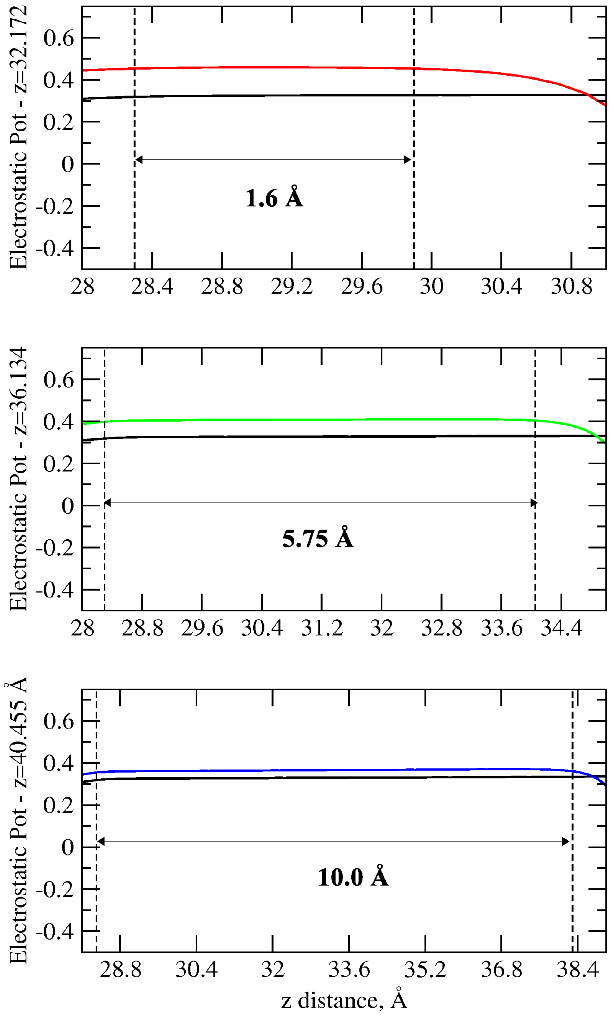

FIG. S6. **Assessing the supercell dimension perpendicular to the gold surface**. Average electrostatic potential in the direction perpendicular to the surface for the different cell dimensions probed. The black line is the reference value obtained for the largest value used while the dotted vertical lines indicate the region in space with vanishingly small electron density, $\rho < 0.001$ e/Bohr^3.

the isometric pulling calculation at $\Delta z = 7.6$ Å, which is the last pulling step before final detachment of the molecule from the surface occurs. The value of the distance perpendicular to the Au surface, d, was decreased from the value employed in the structure optimizations for both isometric and isotensional pulling calculations in vacuum, namely $d = 44.597$ Å, in steps of about 4 Å until a value of $d = 32.172$ Å, which was considered the limiting distance as it is only about 5 Å away from the terminal carbon of the unfolded molecule. At each d value a self-consistent electronic structure calculation was performed, thus the total energy, electronic density and electrostatic potential in the direction perpendicular to the

Au surfaces were obtained and analyzed. The results are summarized in Figs. S5 and S6.

As it can be observed, the difference in energies with respect to the periodic simulation supercell with the largest d value are all within ±0.003 eV, which can be considered to be in the order of numerical errors, i.e. meV. When the average electrostatic potential is analyzed in the region for which the electronic density is very small, $\rho < 0.001$ e/Bohr^3 considered to effectively represent vacuum, it displays a flat behavior that gives for the smallest selected d a layer of vacuum of 1.6 Å. Taking into account that this would be the limiting distance to be examined just prior to the complete detachment from the surface, we considered the value of $d = 32.172$ Å large enough for our subsequent isotensional AIMD simulations with fully explicit solvation.

III. EXPLICIT SOLVATION OF THE PEGYLATED AU(111) INTERFACE

The final PEG–TA/Au(111) configuration obtained from the isotensional pulling calculations at 1.6 nN in vacuum as described in detail above was solvated with TIP4P all-atom water molecules using the genbox tool from the GROMACS package (version 4.5.5) [13]. This approach resulted in filling the periodic supercell – having a cell dimension of 32.172 Å perpendicular to the gold surface as determined and validated in the previous section – with a total of 144 H_2O molecules as illustrated in Fig. S7. Molecular dynamics simulations with the OPLS [14] force field were performed in order to relax the solvation environment. A cut-off distance of 0.7 nm was employed for van der Waals interactions, whereas the Coulombic interactions were treated using the particle mesh Ewald method. After energy minimization, a series of molecular dynamics runs at 300 K were carried out, first in the NVT ensemble for 200 ps, with the perpendicular dimension to the Au(111) surface fixed at 32.172 Å, then at isothermal–isobaric conditions with a constant pressure of 1 bar for another 1000 ps in which the box was allowed to relax only in the direction perpendicular to the Au surface, resulting in a final lattice parameter perpendicular to the Au(111) surface of 31.995 Å, and finally an additional 10 ns run again in the NVT ensemble but using the adjusted perpendicular cell dimension. The final configuration after applying this protocol was taken as the initial configuration for the AIMD simulation as described in the following section.

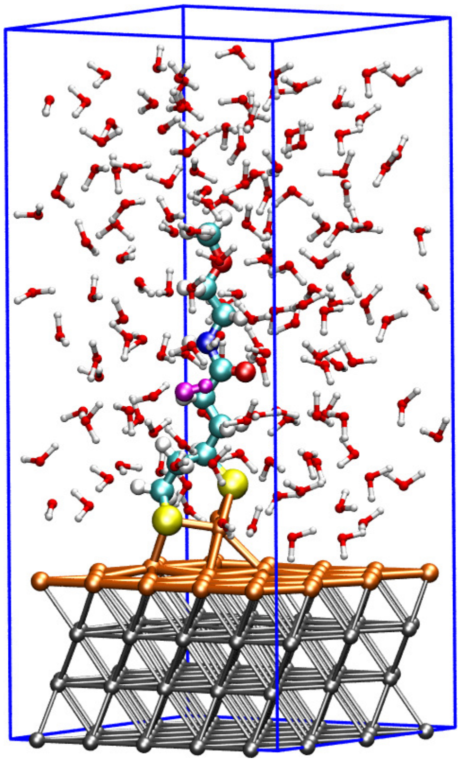

FIG. S7. **Explicit solvation of the pre–stretched PEG–TA/Au(111) interface setup**. The initial structure has been generated based on an isotensional pulling calculation at $F = 1.6$ nN of PEG–TA anchored in vacuum on the Au(111) surface, see panel c of Fig. 2 of the main text for that initial configuration, which is subsequently solvated using 144 water molecules that are depicted; the blue lines are the edges of the periodic supercell used in all AIMD simulations of that fully solvated PEG–TA/Au(111)/water system, see text.

IV. AB INITIO MOLECULAR DYNAMICS SIMULATION SETUP

As mentioned in the main text where the computational details are reported, the AIMD simulations [2] were performed with the CPMD code v. 3.17.1 [15] within the GGA–PBE framework. We recall that this electronic structure setup has been carefully validated in our previous work [8, 9] for closely related gold/thiol interfaces in vacuum. As a result of previous extensive benchmarking [16], adding dispersion corrections to plain PBE such as the widely used D2 or D3 corrections has been shown to *deteriorate* the results (thus significantly increasing the mean absolute deviation) when describing water clusters and hydrogen-bonded systems as probed by the WATER27 benchmark set (see left panel of Fig. 8 in Ref. 16). Based on these findings [16], we refrain from adding any dispersion corrections to the bare

PBE functional, thus following our earlier work on water dissociation [17] (see Supplemental Material therein for discussion). Moreover, the accuracy of plain PBE for estimating energy differences along chemical reactions in liquid water (probing protonation/deprotonation reactions and covalent bond formation in aqueous environment, thus being directly relevant here) has been validated by us [18]. This has been based on comparing our plain PBE results with those obtained with the MP2 method that includes dispersion interaction effects within wavefunction-based electronic structure theories, i.e. without relying on empirical parameterization of dispersion such as the Dn methods. The agreement of the plain PBE energetics with the MP2 benchmark data along reaction pathways in liquid water is convincing as can be judged based on the data compiled in Sec. II of the Electronic Supplementary Material of Ref. 18 and supports the surprising original recommendation [16] of better not adding dispersion corrections to the PBE functional. Aditionally, we note that – based on our own active experience in that field – machine learning potentials (MLPs) also rely on density functional theory, thus offing no advantage in the present case. A notable exception is a recent advance of our group where a high-dimensional neural network MLP based on coupled cluster accuracy, CCSD(T), has been constructed from scratch to describe pure bulk liquid water very accurately [19, 20]. Although this would allow one to go beyond typical density functional accuracy, we (and others) are still far from being able to generalize this sort of coupled cluster accuracy to a system of the complexity as that offered by the present metal-organic-water hybrid. Thus, we (and others) are still bound to using density functional theory for a system of the present complexity for which PBE has been thoroughly validated as explained above.

We finally note in passing that quantum delocalization effects have been studied systematically for a chemical reaction involving H_3O^+ as well as OH^- ions at the interface of water with Pt(111) versus Au(111) surfaces [3]. The authors found pronounced nuclear quantum effects on the Pt(111)/water system while "*minor effects have been observed at the gold interface*" (quoted from the abstract of Ref. [3]). Thus, we refrain from including quantum delocalization effects in the present study of covalent (mechano)chemical reactions subject to high free energy barriers of about 20 to 30 kcal/mol (see the relevant free energy profiles in the central panel of Figure 5 in the main text) that involve in the underlying constrained reaction coordinate (namely the $S \cdots O$ bond distances of the O atom of the attacking nucleophile with respect to the two distinct S atoms of the anchored PEG–TA molecule, see next section) only the motion of heavy atoms with no contributions from proton motion prone to nuclear quantum effects.

V. ENHANCED SAMPLING OF NUCLEOPHILIC ATTACK COMBINED WITH ISOTENSIONAL MECHANICAL STRETCHING

As described in the computational details section of the main text, for the nucleophilic attack of OH^- on either anchoring S atom, an enhanced sampling method has to be employed. The selected method was thermodynamic integration, in which the free energy profile along a suitable reaction coordinate ξ is evaluated by means of a set of constrained (AIMD) simulation runs through

$$\Delta F = -\int_{\xi_\mathrm{i}}^{\xi_\mathrm{f}} f(\xi)\ \mathrm{d}\xi\ , \tag{1}$$

where $f(\xi)$ is the mean force on the constraint while and ξ_i and ξ_f denote the respective reactant and the product states of the chemical reaction. The reaction coordinate in all the isotensional AIMD simulations performed in this work has been the distance between the selected sulfur atom, either S(1) or S(2), and the oxygen atom from the attacking nucleophile, i.e. OH^-.

The upper-left and -right insets in Figure 5 of the main text demonstrate the important aspects of correctly describing both, (i) hydroxide solvation in bulk-like water and (ii) the nucleophilic attack of the S–Au anchor at hybrid metal-organic PEGylated gold interfaces based on our approach. First of all, the PBE functional used in the present work in conjunction with the specific constraint technique [21] (see main text for computational details) is perfectly capable of reproducing the OH^- hydration pattern in aqueous solution which is demonstrated by the upper-left inset in Figure 5 of the main text. The hydration number of OH^- found to be overwhelmingly four (accepted H-bonds) if the hydroxide is far from the molecule, i.e. in the bulk-like environment as relevant in the reactant state. This is in full agreement with the well-established hypercoordination picture of OH^- solvation in aqueous environments where the oxygen site of the hydroxide accepts preferentially 4 H-bonds from four nearby water molecules [22]. Secondly, our approach is also perfectly capable to describe the significant reduction from 4 to 1 hydrating water molecules during the reaction upon product formation as shown by the upper-right inset of that Figure 5. We overall conclude that our present simulation approach correctly describes hydroxide hydration and nucleophilic attack of OH^- in alkaline aqueous solutions.

Sufficient sampling of the average constraint forces as obtained in the blue moon ensemble approach from the Lagrange multipliers along the (AIMD) trajectories is mandatory in order to obtain properly converged free energy profiles along the selected reaction coordinate. To this end, we have performed preliminary force field MD simulations to equilibrate the system (as described above) while applying the desired constant external force. We performed long such simulations and only after those we launched the computationally demanding AIMD simulations. Additionally, since the simulations were performed while applying a rather large initial external force for pre-stretching the long molecule, the "soft" degree of freedom such as bond angles and in particular dihedrals have already reached their limiting "open" values. Thus, the anchored PEG-TA molecule is already in its fully extended state, which is essentially the contour length of the PEG-chain, and is therefore conformationally rigid when the AIMD simulations set in. We demonstrate the convergence of our AIMD sampling protocol in Figs. S8 and S9 for different applied external forces of 1.2 and 2.0 nN, respectively. That force acts on the terminal carbon atom of the PEG-chain and the nucleophile is constrained to attack the sulfur atom 1 (as defined in Figure 1 of the main text) using the methodology as described above in this section. The analysis in Figs. S8 and S9 demonstrates satisfactory convergence of the Lagrange multipliers which underly the free energy profiles that are reported in the main text (and herein).

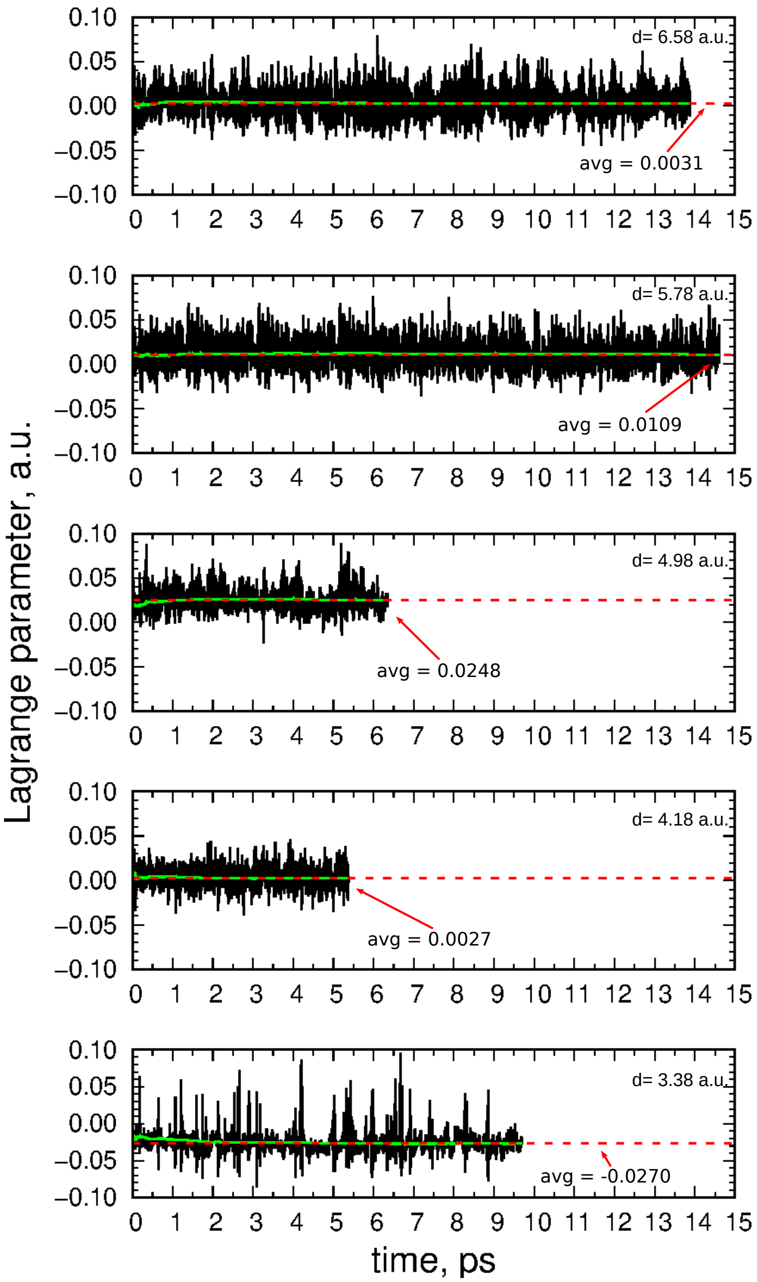

FIG. S8. Lagrange multipliers (in atomic units) as a function of sampling time for a constant external force of $F = 1.2$ nN at five selected points along the reaction path for attack of S(1) by the nucleophile OH^- starting from the reactant state (top panel, constraint distance 6.58 a.u.) and ending in the product state (bottom panel, constraint distance 3.38 a.u.). The black solid line is the Lagrange multiplier at each AIMD step, the green solid line is its running average, and the red dashed line is the overall average (extended in each panel to the right y-axis to enhance visibility).

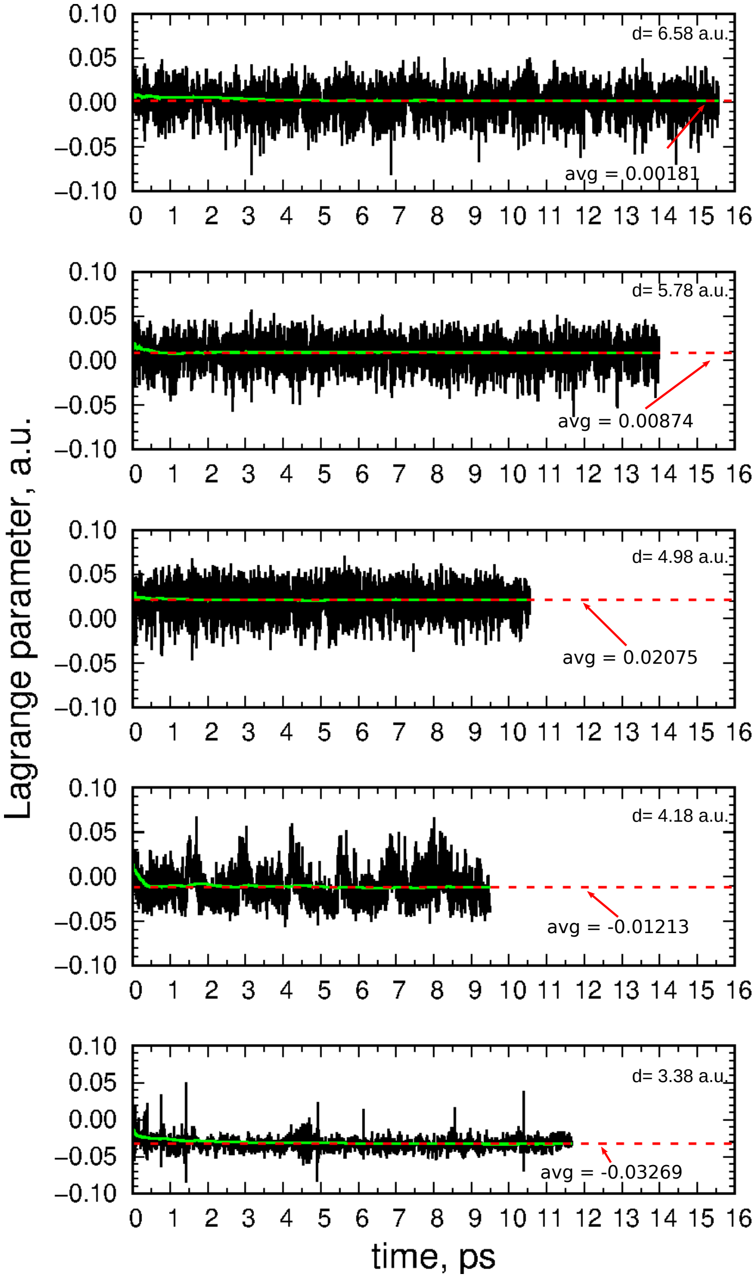

FIG. S9. Lagrange multipliers (in atomic units) as a function of sampling time for a constant external force of $F = 2.0$ nN; see caption of Fig. S8 for labeling.

VI. SUPPORTING ANALYSES OF THE MECHANOCHEMICAL DEGRADATION PROCESS

A. Solvation Effects: Hydration Numbers

In an effort to disclose the impact of water on the purely mechanical degradation mechanism shortly before the anchor breaks, we have analyzed the evolution of the hydration number around both anchoring sulfur atoms and the relevant gold atoms, little before and after detachment at forces of $F = 3.2$ and 3.4 nN. In Fig. S10 bond distances and hydration number of both sulfur atoms are shown shortly before the process of detachment and slightly after the reaction takes place. Top two panels present the situation at $F = 3.4$ nN while the two bottom ones are for 3.2 nN. Three bond lengths are displayed, namely S(1)–Au(3) (red line), S(2)–Au(2) (black line) and Au(3)–Au(2) (brown line). One can immediately see that the process of detachment starts around AIMD step 3000, where for the lower force (3.2 nN) two bonds are breaking almost simultaneously, namely S(2)–Au(2) and Au(3)–Au(2), i.e. one sulfur–gold and one gold–gold bond, thus resulting in gold atom Au(3) being removed from the surface together with the PEG-TA molecule. This leads to the creation of a 6–membered ring where Au(3) has been extracted from the surface and inserted in the thioctic acid TA, see the configuration snapshot to the right of the lower two panels of Fig. S10. At the higher force, $F = 3.4$ nN, a totally different scenario is observed, with two sulfur–gold bonds breaking essentially at the same time, namely S(1)–Au(3) and S(2)–Au(2). This event leaves the sulfur atom S(2) only bonded with one gold atom Au(3) instead of two for a short time, and this remaining bond is then easily broken at the applied force, which finally leaves both gold atoms at the surface.

Refined analysis is based on computing the hydration numbers of the two anchoring sulfur atoms due to water molecules obtained from counting the number of hydrogen atoms from water molecules within a suitable distance cutoff of 2.9 Å from the respective sulfur atom as depicted in Fig. S10 during the very process of detachment. While at the lower force, $F = 3.2$ nN, before final detachment of the molecule occurs, both sulfur atoms have similar hydration numbers, while after rupture the S(1) sulfur is better solvated. At the higher force, 3.4 nN, the situation is the opposite and in this case the sulfur atom S(1) is better solvated than S(2) before the rupture starts, while they acquire a quite similar solvation

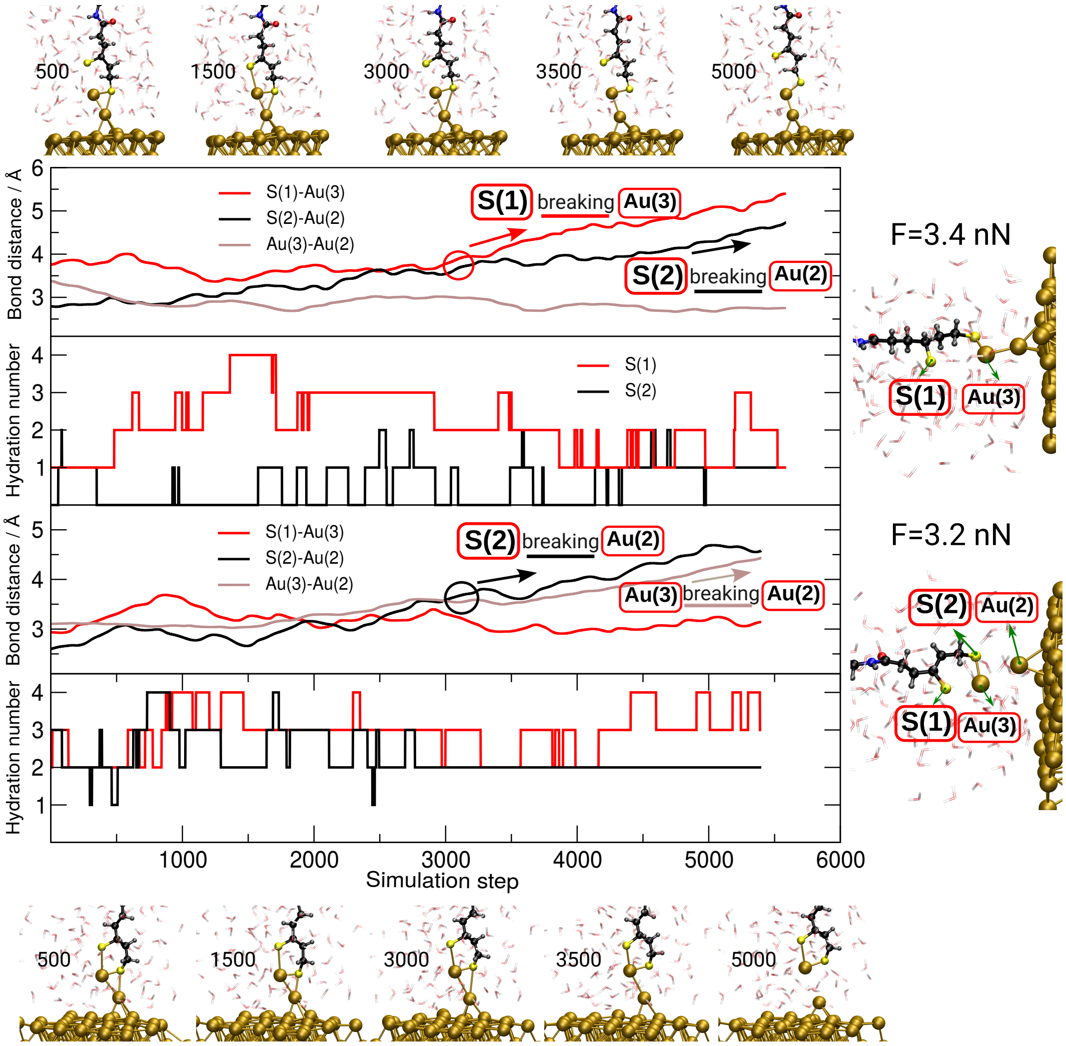

FIG. S10. Top two panels at $F = 3.4$ nN and bottom two panels at $F = 3.2$ nN: Left hand side: Evolution of the hydration numbers of sulfur atoms S(1) (red line) and S(2) (black line) and the bond distances S(1)–Au(3) (red line), S(2)–Au(2) (black line) and Au(3)-Au(2) (brown line) shortly before (AIMD steps up to 3000) and after (beyond 3000 steps) the breaking event. Right hand side: Representative configurations showing the resulting different scenarios, sampled shortly before detachment at the two mechanical forces as indicated.

shell after detachment. We refer to the main text, in particular to Fig. 4 therein and its discussion, for additional statistical analysis of the hydration of the two sulfur atoms by water molecules.

Last but not least, also changes in the solvation shells of the two involved gold atoms are analyzed in Fig. S11. The overall hydration of gold atom Au(3) close to detachment is

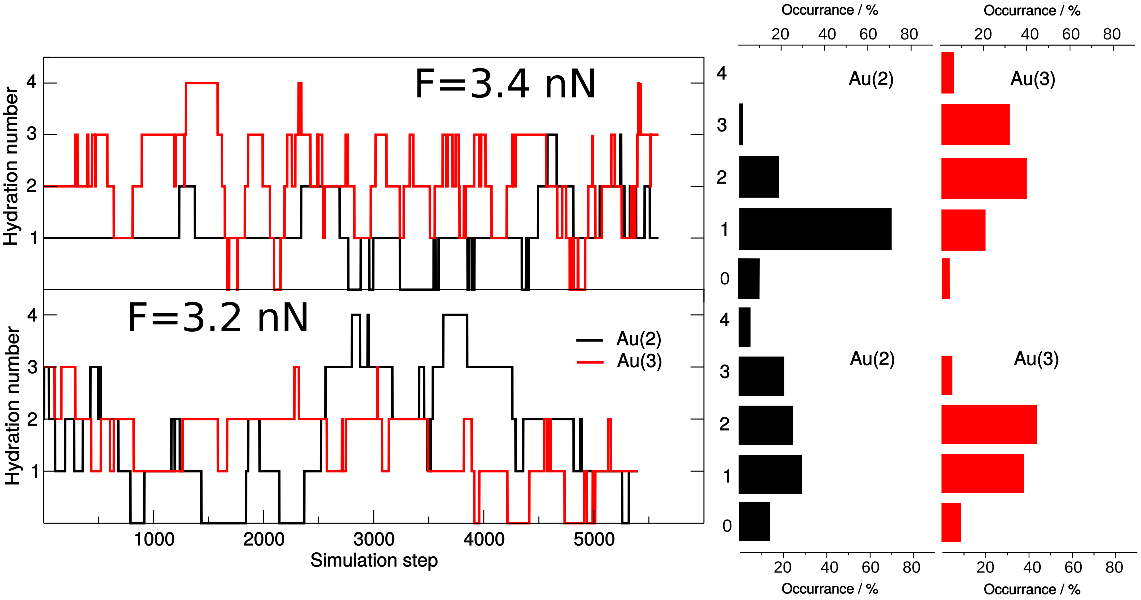

FIG. S11. Hydration numbers of gold atoms Au(3) (red line) and Au(2) (black line) close to breaking the PEG–TA/Au(111) anchor similar to the analyses in Figs. S10. Right insets: Total hydration numbers of both gold atoms at the two respective forces.

quite similar at the two forces, still one can see that Au(3) is slightly better solvated at the higher force. This is due to the fact that at $F = 3.4$ nN the Au(3) atom is not extracted from the surface, rather it is fully exposed to solvent as it is slightly pulled over the surface such that it stays nicely solvated by water at the end. In contrast, at $F = 3.2$ nN, Au(3) gets fully detached from the surface and incorporated into the 6–membered disulfide ring of the thioctic acid TA.

The important observation is that while at the lower force both gold atoms have decreased their solvation in comparison to the higher force, after the breaking process the hydration of both gold atoms has increased. What it seen is that at 3.2 nN the solvation of Au(2) is growing before the detachment process occurs, so once the Au(2) atom is better solvated, the Au(2)–Au(3) bond gets weakened and, thus, is likely to break as observed where Au(2) remains in the surface while Au(3) gets carried away with the detached molecule.

B. Reactivity Effects: Sulfur versus Gold Interactions

In the following, we analyze in detail the scenarios presented in Figs. 8 and 9 in the main text.

1. *S(2) Reactivity at 1.2 nN*

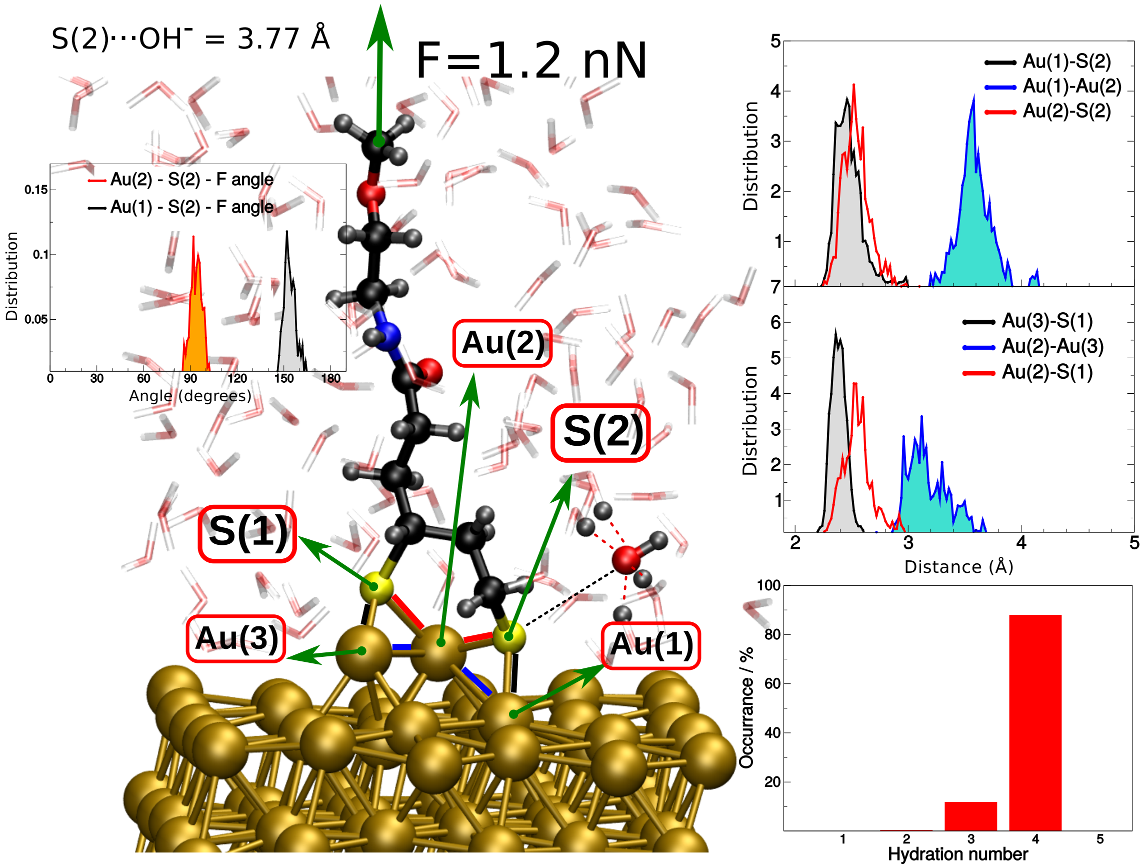

FIG. S12. **Analysis of sulfur S(2)–gold linkage at $F = 1.2$ nN with distance constraint S(2)$\cdots$ OH$^-$=3.77Å.** Left inset: Distribution alignment of gold-sulfur bonds Au(2)-S(2) (orange line) and Au(1)-S(2) (gray line). Top right panel: Distributions of the bond lengths Au(1)-S(2) (black line), Au(1)-Au(2) (blue line) and Au(2)-S(2) (red line) for the present distance constraint. Middle right panel: Distributions of the bond lengths Au(3)-S(1) (black line), Au(2)-Au(3) (blue line) and Au(2)-S(1) (red line) for the present distance constraint. Bottom right inset: Distribution of hydration numbers of oxygen atom from OH$^-$(aq).

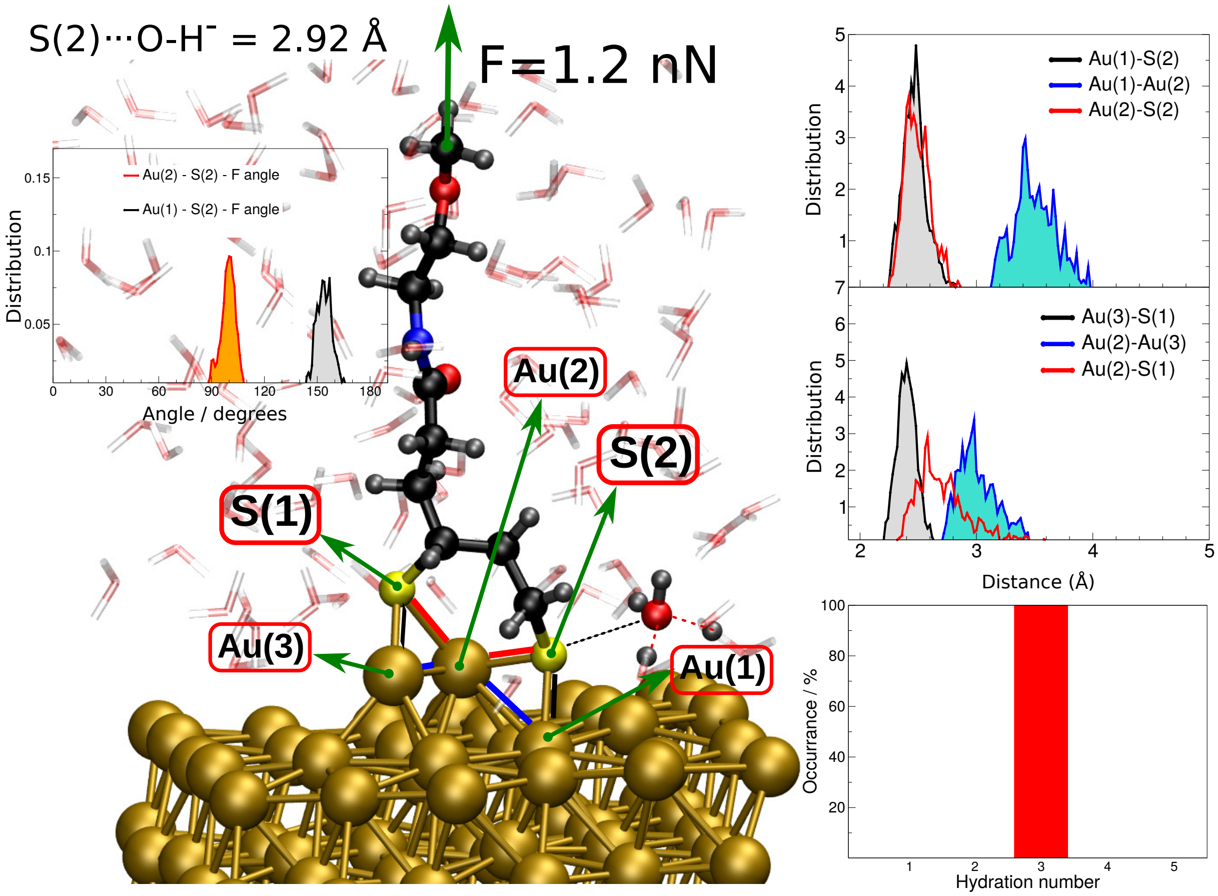

FIG. S13. **Analysis of sulfur S(2)–gold linkage at $F = 1.2$ nN with distance constraint S(2)$\cdots$ OH$^-$=2.92Å.** Left inset: Distribution alignment of gold-sulfur bonds Au(2)-S(2) (orange line) and Au(1)-S(2) (gray line). Top right panel: Distributions of the bond lengths Au(1)-S(2) (black line), Au(1)-Au(2) (blue line) and Au(2)-S(2) (red line) for the present distance constraint. Middle right panel: Distributions of the bond lengths Au(3)-S(1) (black line), Au(2)-Au(3) (blue line) and Au(2)-S(1) (red line) for the present distance constraint. Bottom right inset: Distribution of hydration numbers of oxygen atom from OH$^-$(aq).

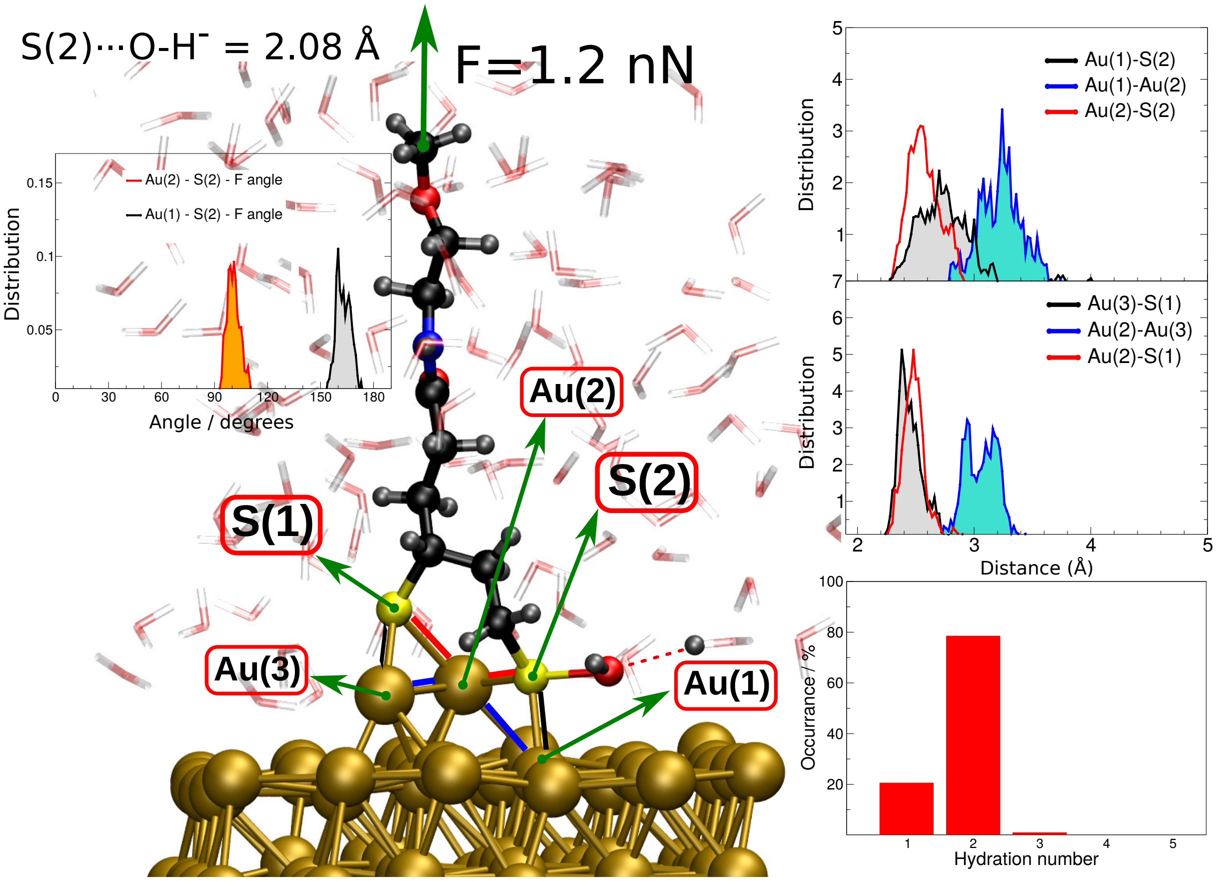

FIG. S14. **Analysis of sulfur S(2)–gold linkage at $F = 1.2$ nN with distance constraint S(2)$\cdots$ OH$^-$=2.08Å.** Left inset: Distribution alignment of gold-sulfur bonds Au(2)-S(2) (orange line) and Au(1)-S(2) (gray line). Top right panel: Distributions of the bond lengths Au(1)-S(2) (black line), Au(1)-Au(2) (blue line) and Au(2)-S(2) (red line) for the present distance constraint. Middle right panel: Distributions of the bond lengths Au(3)-S(1) (black line), Au(2)-Au(3) (blue line) and Au(2)-S(1) (red line) for the present distance constraint. Bottom right inset: Distribution of hydration numbers of oxygen atom from OH$^-$(aq).

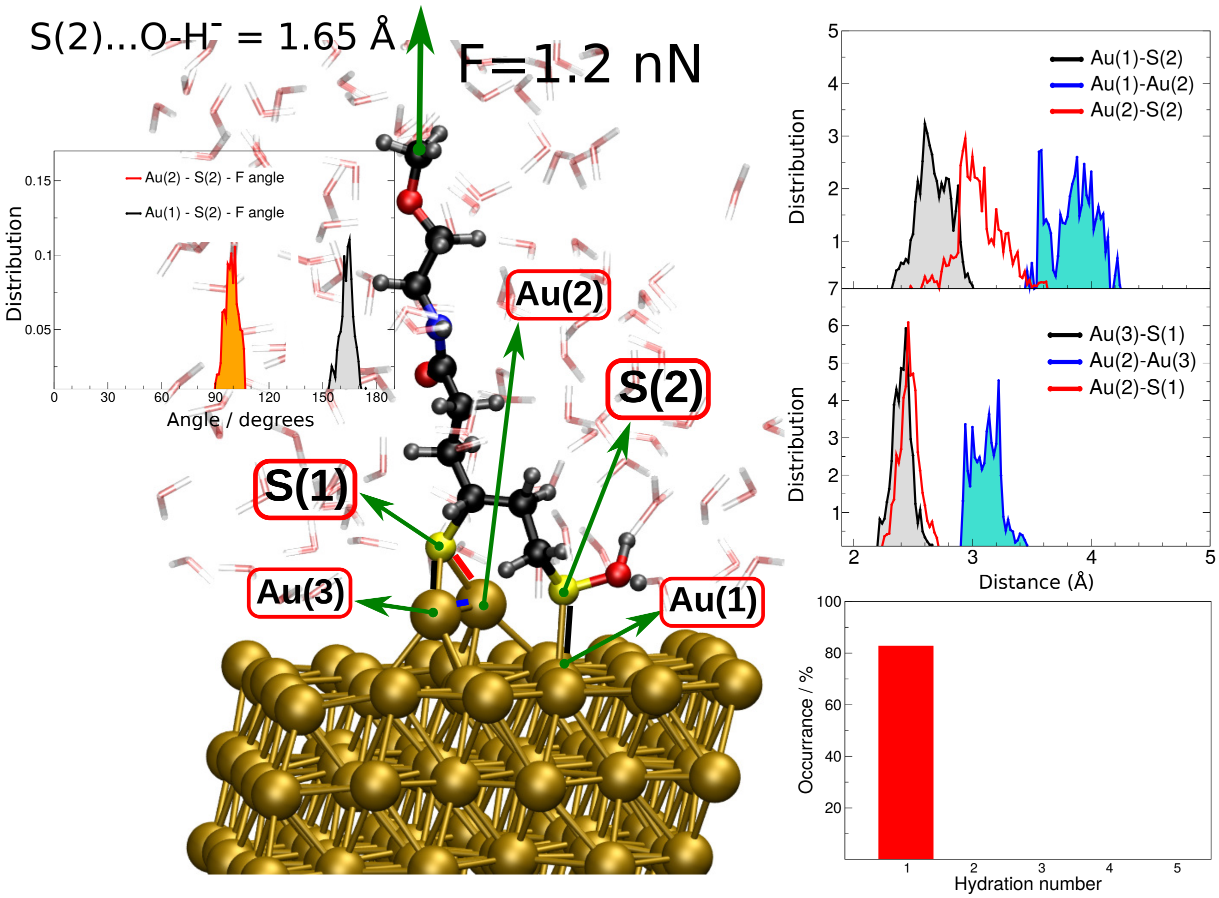

FIG. S15. **Analysis of sulfur S(2)–gold linkage at F = 1.2 nN with distance constraint S(2)$\cdots$ OH$^-$=1.65Å.** Left inset: Distribution alignment of gold-sulfur bonds Au(2)-S(2) (orange line) and Au(1)-S(2) (gray line). Top right panel: Distributions of the bond lengths Au(1)-S(2) (black line), Au(1)-Au(2) (blue line) and Au(2)-S(2) (red line) for the present distance constraint. Middle right panel: Distributions of the bond lengths Au(3)-S(1) (black line), Au(2)-Au(3) (blue line) and Au(2)-S(1) (red line) for the present distance constraint. Bottom right inset: Distribution of hydration numbers of oxygen atom from OH$^-$(aq).

2. *S(2) Reactivity at 2.0 nN*

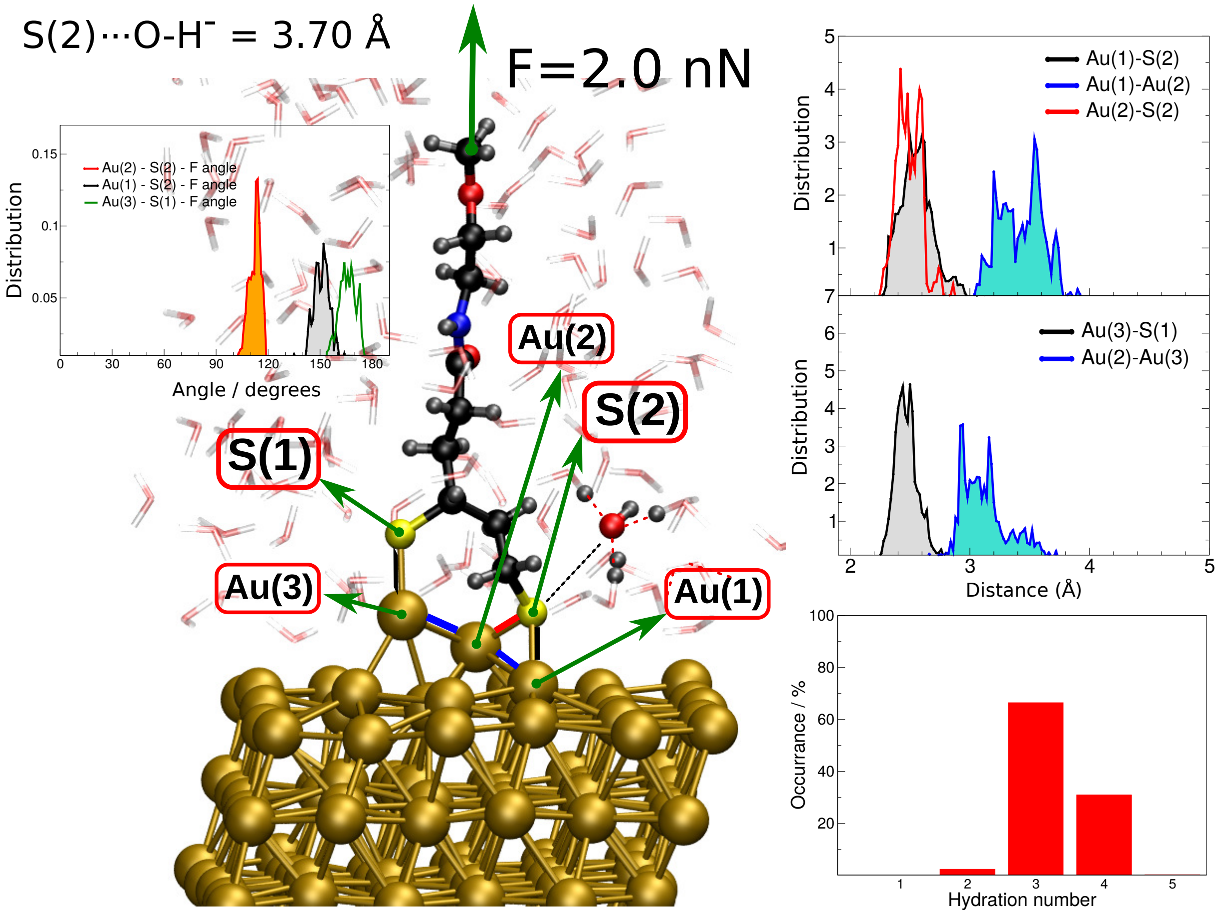

FIG. S16. **Analysis of sulfur S(2)–gold linkage at $F = 2.0$ nN with distance constraint S(2)$\cdots$ OH$^-$=3.70Å.** Left inset: Distribution alignment of gold-sulfur bonds Au(2)-S(2) (orange line), Au(1)-S(2) (gray line), and Au(3)-S(1) (green line). Top right panel: Distributions of the bond lengths Au(1)-S(2) (black line), Au(1)-Au(2) (blue line), and Au(2)-S(2) (red line) for the present distance constraint. Middle right panel: Distributions of the bond lengths Au(3)-S(1) (black line), Au(2)-Au(3) (blue line) for the present distance constraint. Bottom right inset: Distribution of hydration numbers of oxygen atom from OH$^-$(aq).

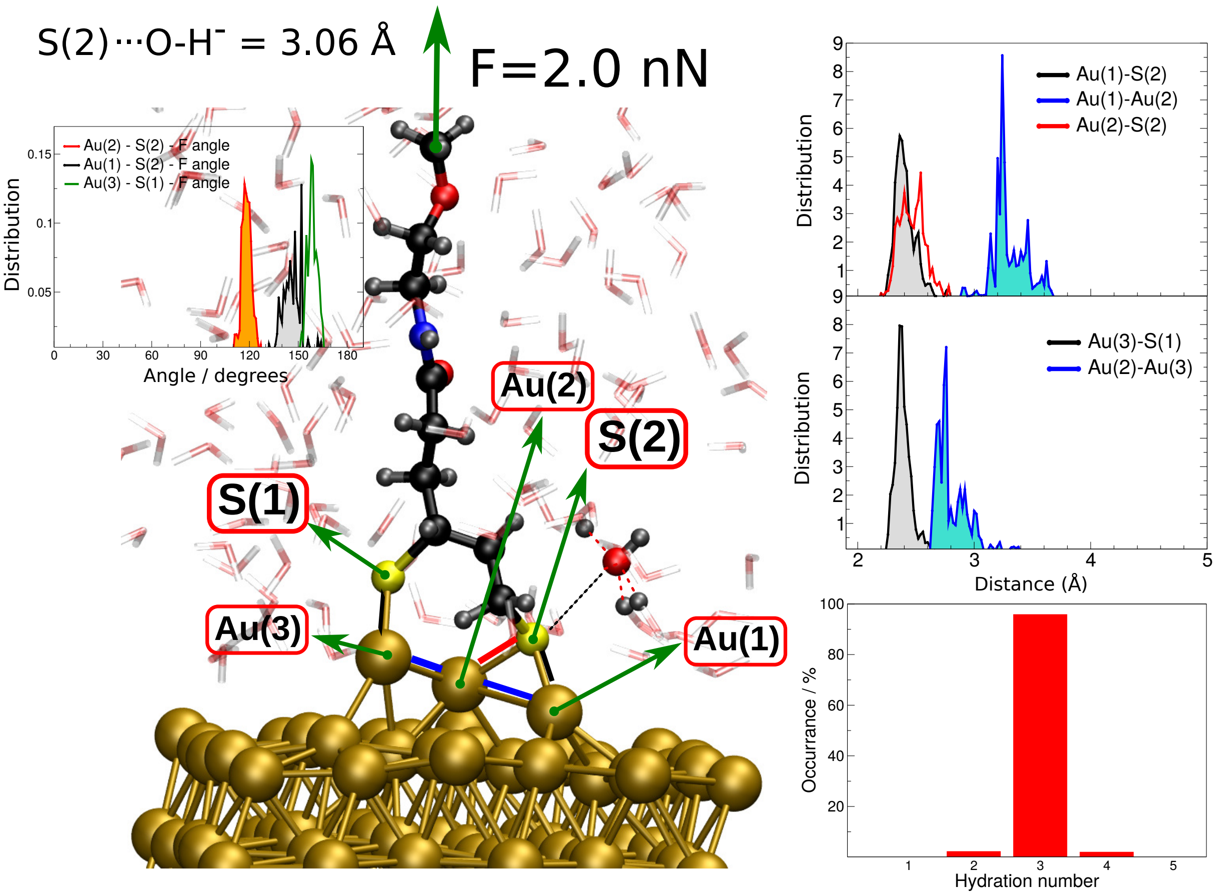

FIG. S17. **Analysis of sulfur S(2)–gold linkage at $F = 2.0$ nN with distance constraint S(2)$\cdots$ OH$^-$=3.06Å.** Left inset: Distribution alignment of gold-sulfur bonds Au(2)-S(2) (orange line), Au(1)-S(2) (gray line), and Au(3)-S(1) (green line). Top right panel: Distributions of the bond lengths Au(1)-S(2) (black line), Au(1)-Au(2) (blue line), and Au(2)-S(2) (red line) for the present distance constraint. Middle right panel: Distributions of the bond lengths Au(3)-S(1) (black line), Au(2)-Au(3) (blue line) for the present distance constraint. Bottom right inset: Distribution of hydration numbers of oxygen atom from OH$^-$(aq).

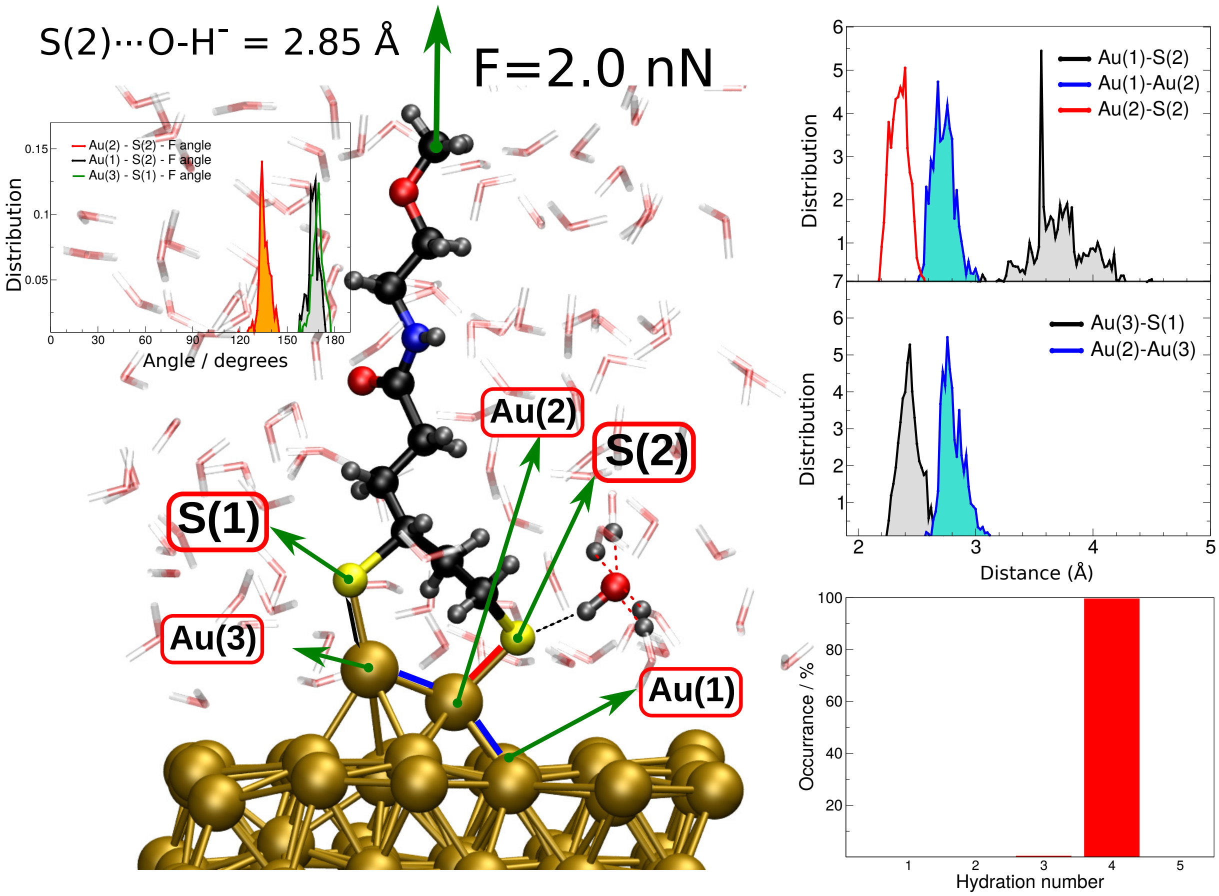

FIG. S18. **Analysis of sulfur S(2)–gold linkage at F = 2.0 nN with distance constraint S(2)$\cdots$ OH$^-$=2.85Å.** Left inset: Distribution alignment of gold-sulfur bonds Au(2)-S(2) (orange line), Au(1)-S(2) (gray line), and Au(3)-S(1) (green line). Top right panel: Distributions of the bond lengths Au(1)-S(2) (black line), Au(1)-Au(2) (blue line), and Au(2)-S(2) (red line) for the present distance constraint. Middle right panel: Distributions of the bond lengths Au(3)-S(1) (black line), Au(2)-Au(3) (blue line) for the present distance constraint. Bottom right inset: Distribution of hydration numbers of oxygen atom from OH$^-$(aq).

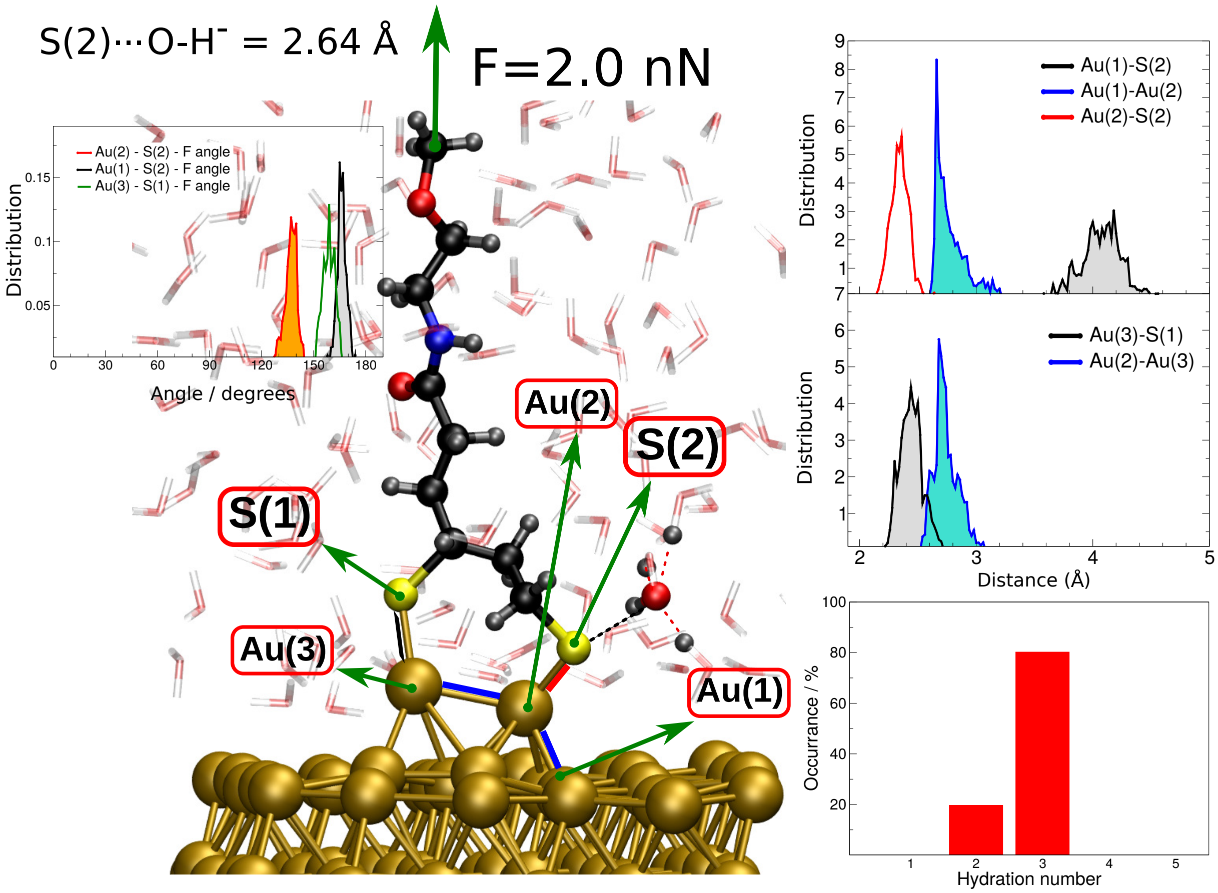

FIG. S19. **Analysis of sulfur S(2)–gold linkage at F = 2.0 nN with distance constraint S(2)$\cdots$ OH$^-$=2.64Å.** Left inset: Distribution alignment of gold-sulfur bonds Au(2)-S(2) (orange line), Au(1)-S(2) (gray line), and Au(3)-S(1) (green line). Top right panel: Distributions of the bond lengths Au(1)-S(2) (black line), Au(1)-Au(2) (blue line), and Au(2)-S(2) (red line) for the present distance constraint. Middle right panel: Distributions of the bond lengths Au(3)-S(1) (black line), Au(2)-Au(3) (blue line) for the present distance constraint. Bottom right inset: Distribution of hydration numbers of oxygen atom from OH$^-$(aq).

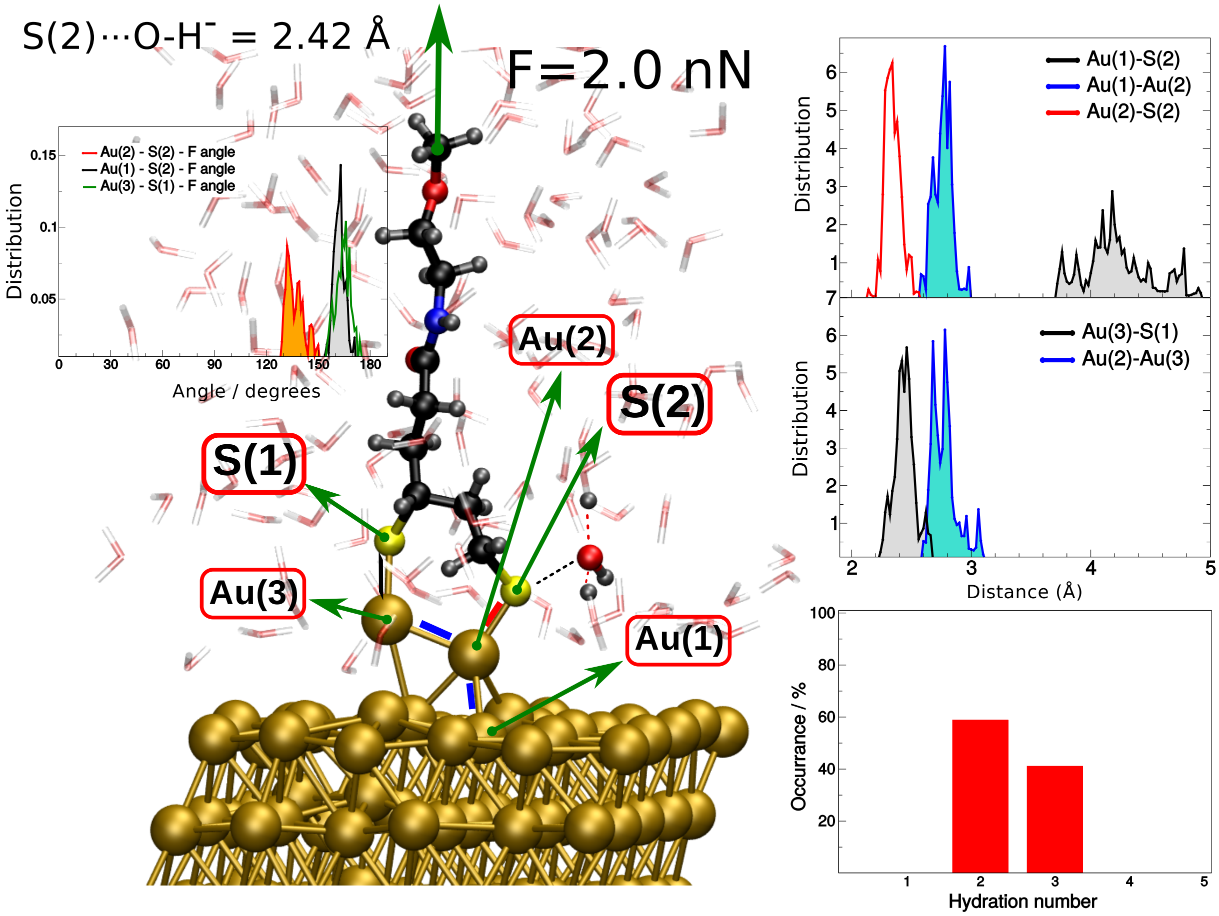

FIG. S20. **Analysis of sulfur S(2)–gold linkage at $F = 2.0$ nN with distance constraint S(2)$\cdots$ OH$^-$=2.42Å.** Left inset: Distribution alignment of gold-sulfur bonds Au(2)-S(2) (orange line), Au(1)-S(2) (gray line), and Au(3)-S(1) (green line). Top right panel: Distributions of the bond lengths Au(1)-S(2) (black line), Au(1)-Au(2) (blue line), and Au(2)-S(2) (red line) for the present distance constraint. Middle right panel: Distributions of the bond lengths Au(3)-S(1) (black line), Au(2)-Au(3) (blue line) for the present distance constraint. Bottom right inset: Distribution of hydration numbers of oxygen atom from OH$^-$(aq).

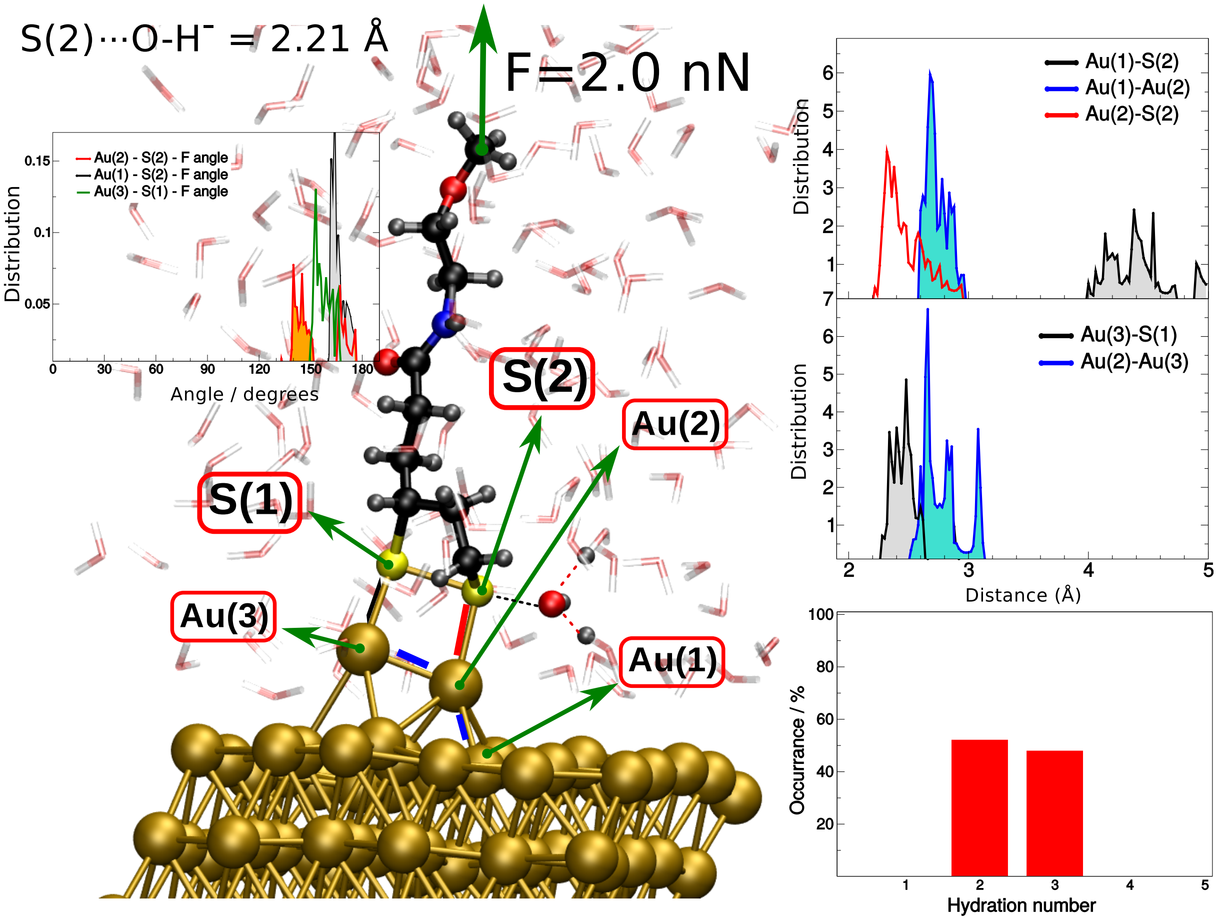

FIG. S21. **Analysis of sulfur S(2)–gold linkage at $F = 2.0$ nN with distance constraint S(2)$\cdots$ OH$^-$=2.21Å.** Left inset: Distribution alignment of gold-sulfur bonds Au(2)-S(2) (orange line), Au(1)-S(2) (gray line), and Au(3)-S(1) (green line). Top right panel: Distributions of the bond lengths Au(1)-S(2) (black line), Au(1)-Au(2) (blue line), and Au(2)-S(2) (red line) for the present distance constraint. Middle right panel: Distributions of the bond lengths Au(3)-S(1) (black line), Au(2)-Au(3) (blue line) for the present distance constraint. Bottom right inset: Distribution of hydration numbers of oxygen atom from OH$^-$(aq).

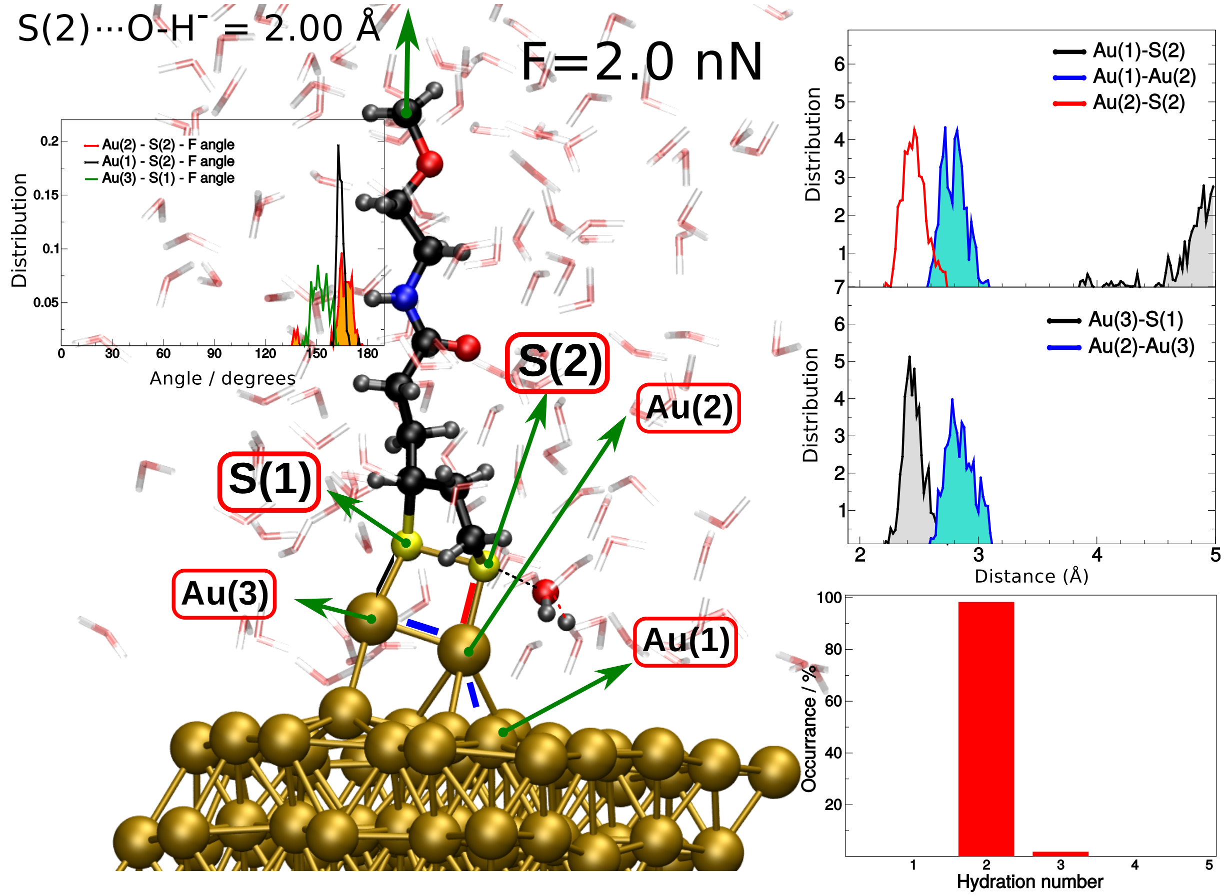

FIG. S22. **Analysis of sulfur S(2)–gold linkage at $F = 2.0$ nN with distance constraint S(2)$\cdots$ OH$^-$=2.00Å.** Left inset: Distribution alignment of gold-sulfur bonds Au(2)-S(2) (orange line), Au(1)-S(2) (gray line), and Au(3)-S(1) (green line). Top right panel: Distributions of the bond lengths Au(1)-S(2) (black line), Au(1)-Au(2) (blue line), and Au(2)-S(2) (red line) for the present distance constraint. Middle right panel: Distributions of the bond lengths Au(3)-S(1) (black line), Au(2)-Au(3) (blue line) for the present distance constraint. Bottom right inset: Distribution of hydration numbers of oxygen atom from OH$^-$(aq).

3. S(2) Reactivity at 2.0 nN: 5–membered versus 6–membered ring

Since we found two strikingly different but isoenergetic decomposition pathways at $F =$ 2.0 nN as mentioned in the main text, the first one resulting in extracting a 5–membered disulfide ring with no gold atoms detached from the surface (see the Path 2 data in Fig. 7 of the main text) and the second one leading to a 6–membered ring with one gold atom detached from the surface (see the Path 1 data in Fig. 7 of the main text) we now analyze in detail the structural parameters close to the sulfur–gold junction to rationalize this finding.

The important parameters are reported in Fig. 7 of the main text where firstly the evolution of the S(1)$\cdots$S(2) distances during the final steps of the reaction is monitored for both pathways (see graphs below the configuration analyses along the two pathways). One can immediately see that for Path 2 (yielding the 5–membered ring, see right graphs), from around 300–400 fs on we observe fast formation of the disufide bond as heralded by a S–S bond length that fluctuates around roughly 2.2–2.3 Å at about 600 fs and beyond. Key is to monitor the dynamics of the gold adatoms close to the junction, i.e. Au(2) and Au(3) according to our labeling. Simultaneously with this bond formation in the molecule a single gold atom, Au(3), is progressively elevating above the gold surface (red line in the right-middle graph) while the other one, Au(2), gets even more tightly bonded to the gold surface which is highlighted by the yellow shading; see the inset in the top panel for atom labeling. Concurrently to these changes, a markedly different coordination pattern is observed for these two gold atoms (right-bottom graph): Au(2) exhibits significantly increased coordination with the other gold atoms (black line: 4–5 gold atoms in the first shell) implying that it is more tightly embedded in the surface, whereas Au(3) exhibits weaker coordination with the surface (red line: 3–2 gold atoms) during that phase. However, setting in at about 600 fs when when both sulfur atoms are bonded and form the disulfide bond (and thus the 5–membered ring), both gold atoms begin to place themselves at the same height above the gold surface (right-middle graph) and simultaneously their coordination patterns starts to become similar as well with about 4 other gold atoms around them (right-bottom graph). We thus see that these two quite mobile Au adatoms move at room temperature in a correlated manner such that disulfide bond formation is possible.

Along the pathway 1 analyzed analogously in the left graphs, leading to the 6–membered ring with extraction of gold atom Au(3), the adatom reorganization is different. In this pathway we observed early on that the S(1)···S(2) distance evolution is different. Importantly, we must consider the dynamics of the gold adatoms. We observe that the two relevant gold atoms Au(2) and Au(3) are much higher on top of the Au(111) surface around them (compare their different height scales in the right-middel versus the left-middle graphs), thus they are both more detached from the surface. One of them, Au(3), systematically departs from the surface (red line in the left-middle graph) and readily inserts into the rather open S(1)···S(2) contact (which is clearly not forming an S–S bond, compare to the left-top graph after 600 fs), which concurrently opens up even more at about 600 fs (left-upper graph). Once again, the dynamics of the gold coordination numbers provides valuable mechanistic insights: While Au(2) which ultimately remains attached to the surface is nicely coordinated throughout and thus firmly bonded within the gold surface with about 4 gold neigbhors, the detached Au(3) is found to be very weakly coordinated, thus loosely bonded within the gold surface up to detachment. This scenario of adatom dynamics is totaly different from that observed along the other pathway: Here, the adatom mobility at 300 K generates a situation where one gold atom sticks much out of the surface and, being so exposed, can readily insert into the S(1)···S(2) contact to form two Au–S bonds which leads to the 6–membered ring with its covalent S(1)–Au(3)–S(2) bonding motif.

Our observation of pronounced coordination number fluctuations of these exposed gold adatoms is fully consistent with the well-established fluxional character of gold nanoparticles at room temperature. [23] In addition, this fluxionality has been shown to impact the reactivity of gold clusters at the level of reaction pathways and barriers. [24] As a result, different reaction pathways leading to different reaction products can be opened depending on fluctuations as a result of the high mobility in particular of low–coordinated gold atoms. In the present case, we find that the fluxionality and thus mobility of the low–coordinated gold adatoms right at the stretched (and thus stressed) metal–molecule junction in aqueous solution at room temperature can lead to different mechanochemical degradation pathways and products.

4. *S(1) Reactivity at 1.2 nN*

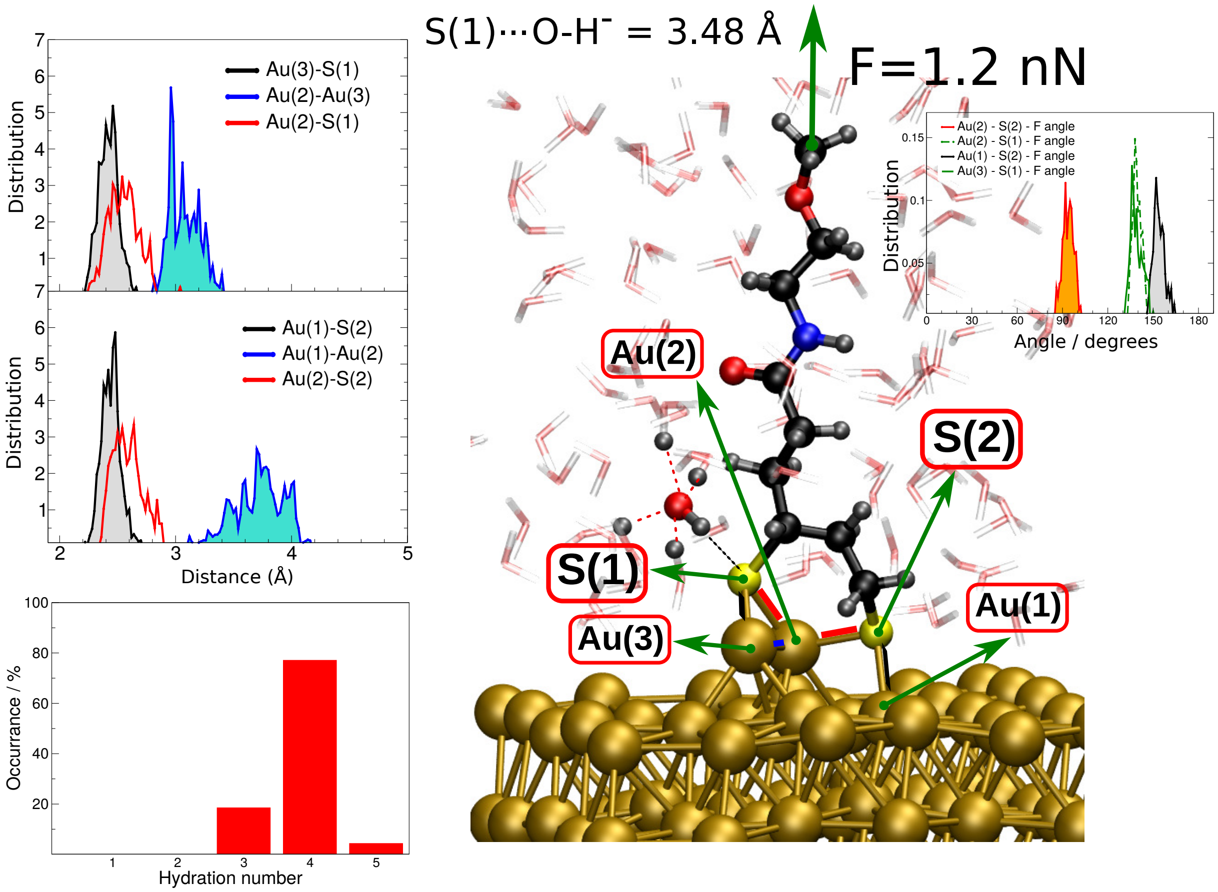

FIG. S23. **Analysis of sulfur S(1)–gold linkage at $F = 1.2$ nN with distance constraint S(1) $\cdots$ OH$^-$=3.48Å.** Right inset: Distribution alignment of gold-sulfur bonds Au(2)-S(2) (orange line), Au(1)-S(2) (gray line), Au(2)-S(1) (dotted green line), and Au(3)-S(1) (green line). Top left panel: Distributions of the bond lengths Au(3)-S(1) (black line), Au(2)-Au(3) (blue line), and Au(2)-S(1) (red line) for the present distance constraint. Middle right panel: Distributions of the bond lengths Au(1)-S(2) (black line), Au(1)-Au(2) (blue line), and Au(2)-S(2) (red line) for the present distance constraint. Bottom right inset: Distribution of hydration numbers of oxygen atom from OH$^-$(aq).

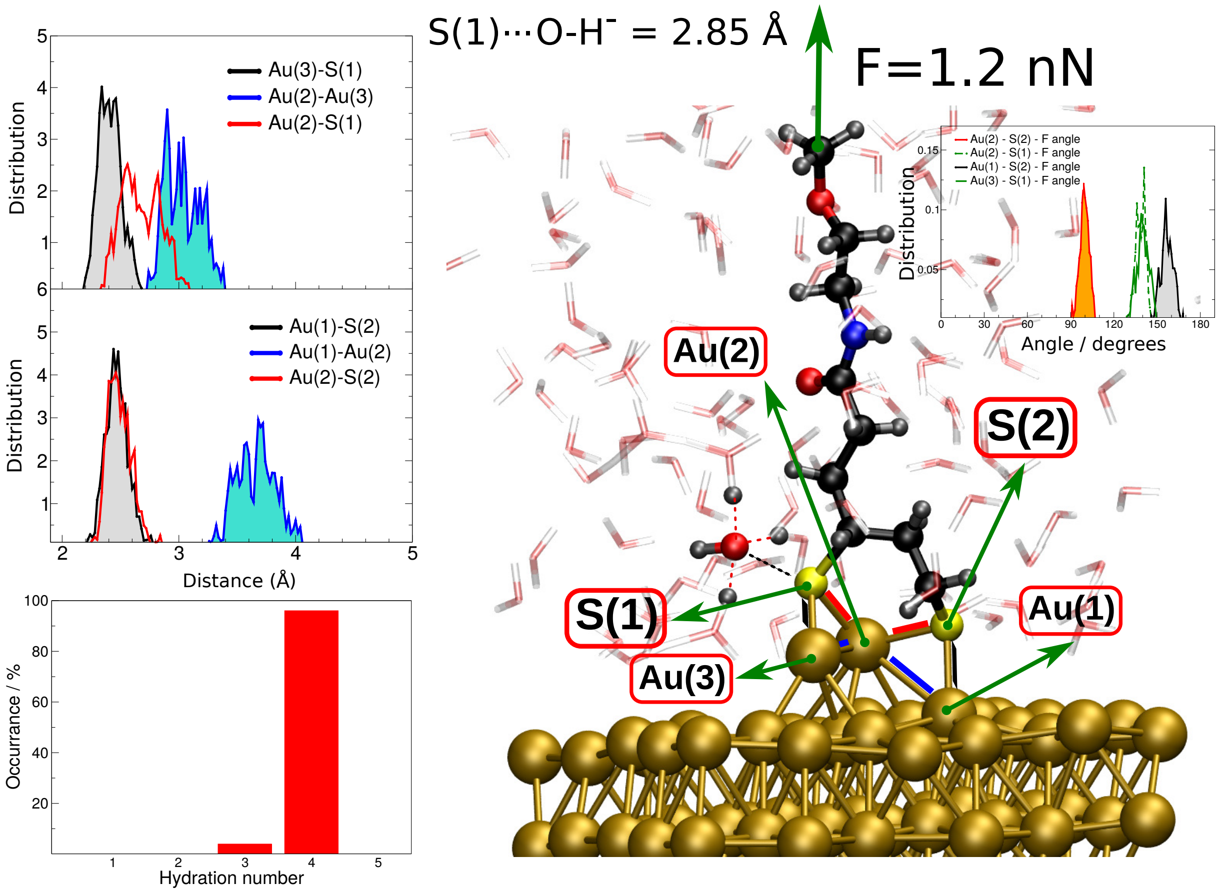

FIG. S24. **Analysis of sulfur S**(1)**–gold linkage at** $F = 1.2$ **nN with distance constraint S**$(1)\cdots$ **OH**$^-$**=2.85Å.** Right inset: Distribution alignment of gold-sulfur bonds Au(2)-S(2) (orange line), Au(1)-S(2) (gray line), Au(2)-S(1) (dotted green line), and Au(3)-S(1) (green line). Top left panel: Distributions of the bond lengths Au(3)-S(1) (black line), Au(2)-Au(3) (blue line), and Au(2)-S(1) (red line) for the present distance constraint. Middle right panel: Distributions of the bond lengths Au(1)-S(2) (black line), Au(1)-Au(2) (blue line), and Au(2)-S(2) (red line) for the present distance constraint. Bottom right inset: Distribution of hydration numbers of oxygen atom from OH$^-$(aq).

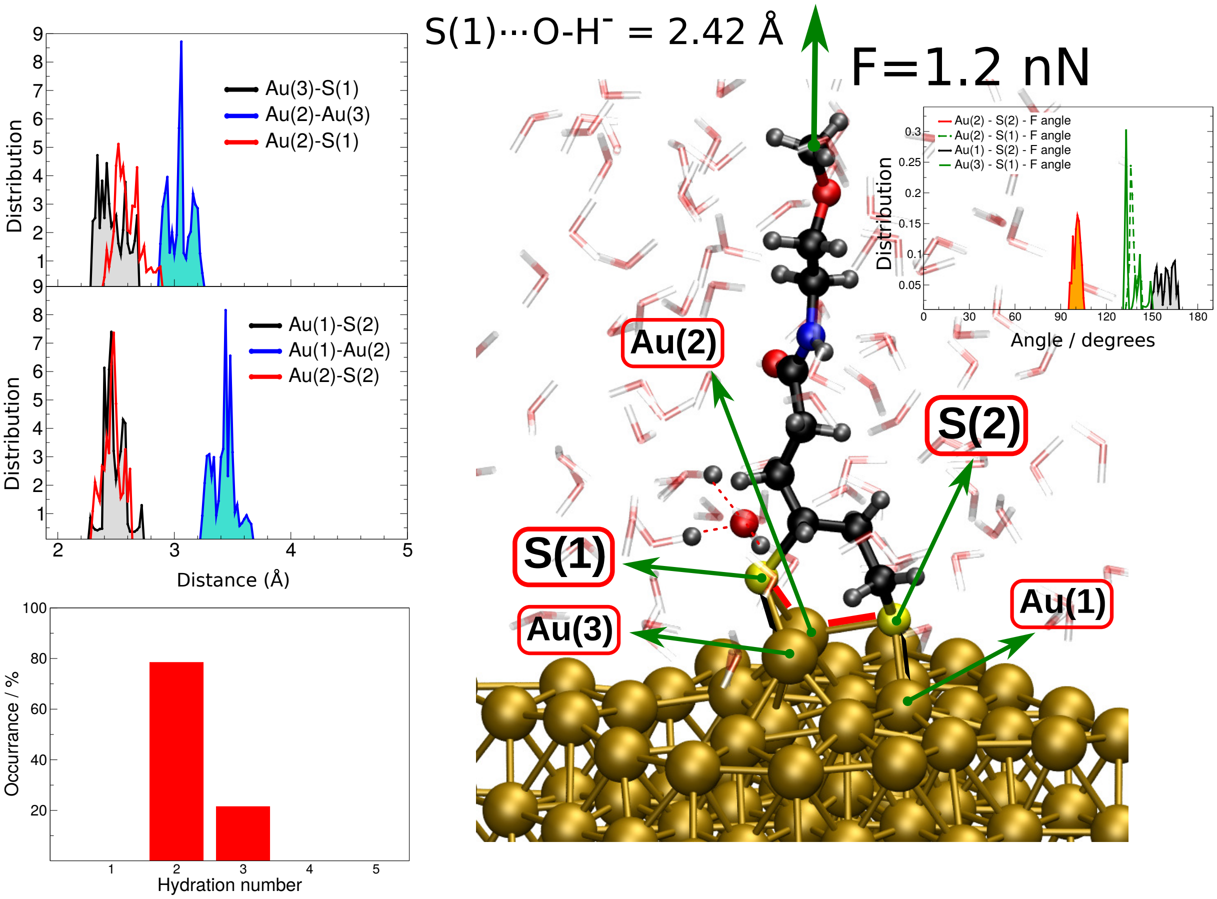

FIG. S25. **Analysis of sulfur S(1)–gold linkage at $F = 1.2$ nN with distance constraint $\mathbf{S(1)\cdots OH^-=2.42}$Å.** Right inset: Distribution alignment of gold-sulfur bonds Au(2)-S(2) (orange line), Au(1)-S(2) (gray line), Au(2)-S(1) (dotted green line), and Au(3)-S(1) (green line). Top left panel: Distributions of the bond lengths Au(3)-S(1) (black line), Au(2)-Au(3) (blue line), and Au(2)-S(1) (red line) for the present distance constraint. Middle right panel: Distributions of the bond lengths Au(1)-S(2) (black line), Au(1)-Au(2) (blue line), and Au(2)-S(2) (red line) for the present distance constraint. Bottom right inset: Distribution of hydration numbers of oxygen atom from OH^-(aq).

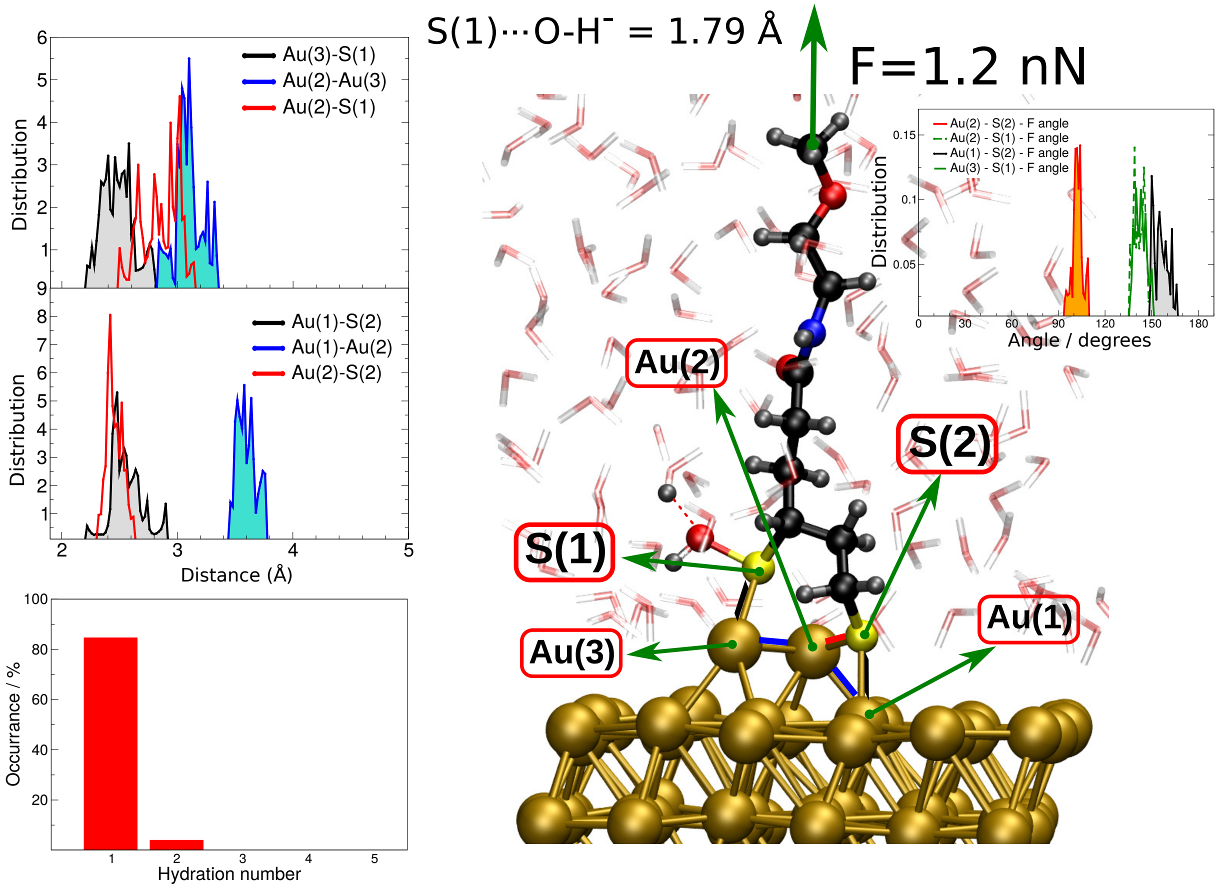

FIG. S26. **Analysis of sulfur S(1)–gold linkage at $F = 1.2$ nN with distance constraint $\mathbf{S(1)\cdots OH^{-}=1.79}$Å.** Right inset: Distribution alignment of gold-sulfur bonds Au(2)-S(2) (orange line), Au(1)-S(2) (gray line), Au(2)-S(1) (dotted green line), and Au(3)-S(1) (green line). Top left panel: Distributions of the bond lengths Au(3)-S(1) (black line), Au(2)-Au(3) (blue line), and Au(2)-S(1) (red line) for the present distance constraint. Middle right panel: Distributions of the bond lengths Au(1)-S(2) (black line), Au(1)-Au(2) (blue line), and Au(2)-S(2) (red line) for the present distance constraint. Bottom right inset: Distribution of hydration numbers of oxygen atom from OH^{-}(aq).

5. *S(1) Reactivity at 2.0 nN*

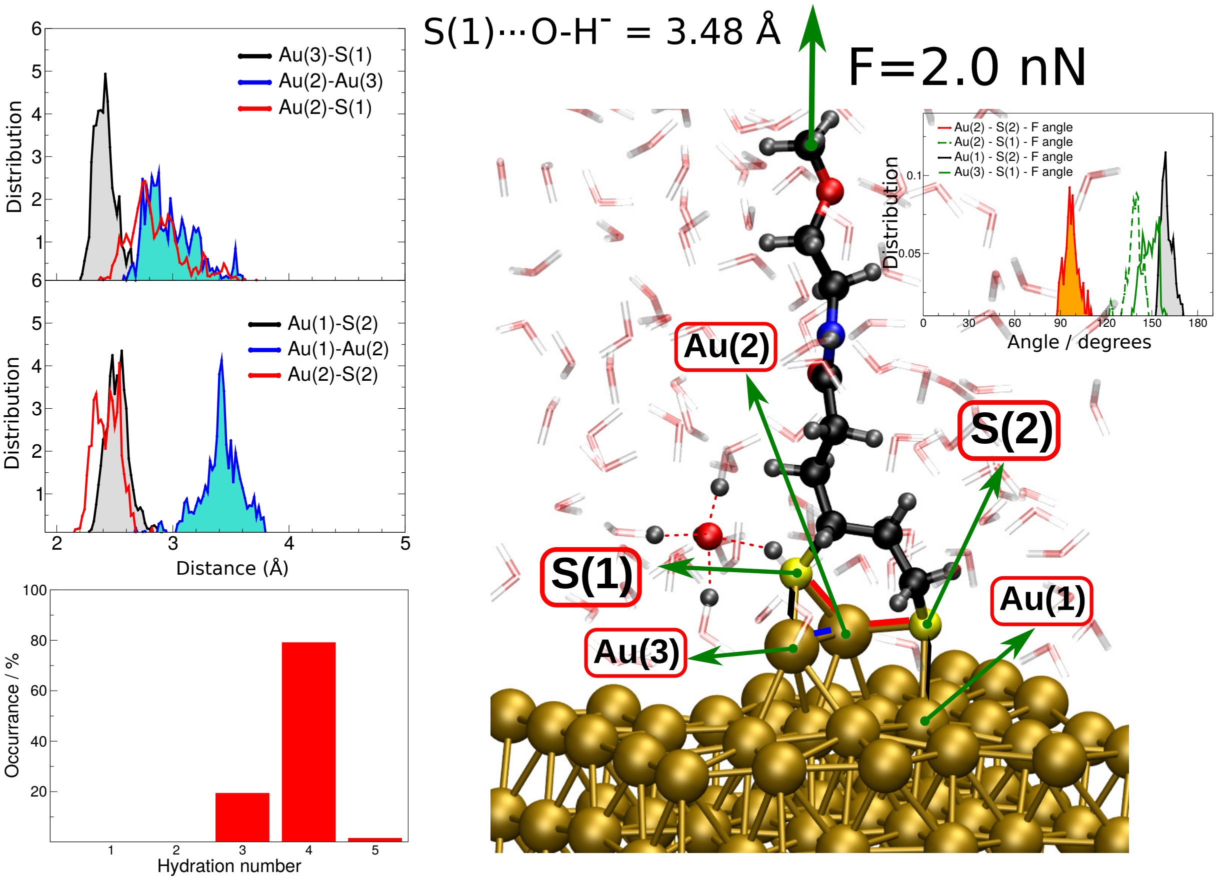

FIG. S27. **Analysis of sulfur S**(1)**–gold linkage at** F = 2.0 **nN with distance constraint S**(1) $\cdots$ **OH**$^-$**=3.48Å.** Right inset: Distribution alignment of gold-sulfur bonds Au(2)-S(2) (orange line), Au(1)-S(2) (gray line), Au(2)-S(1) (dotted green line), and Au(3)-S(1) (green line). Top left panel: Distributions of the bond lengths Au(3)-S(1) (black line), Au(2)-Au(3) (blue line), and Au(2)-S(1) (red line) for the present distance constraint. Middle right panel: Distributions of the bond lengths Au(1)-S(2) (black line), Au(1)-Au(2) (blue line), and Au(2)-S(2) (red line) for the present distance constraint. Bottom right inset: Distribution of hydration numbers of oxygen atom from OH$^-$(aq).

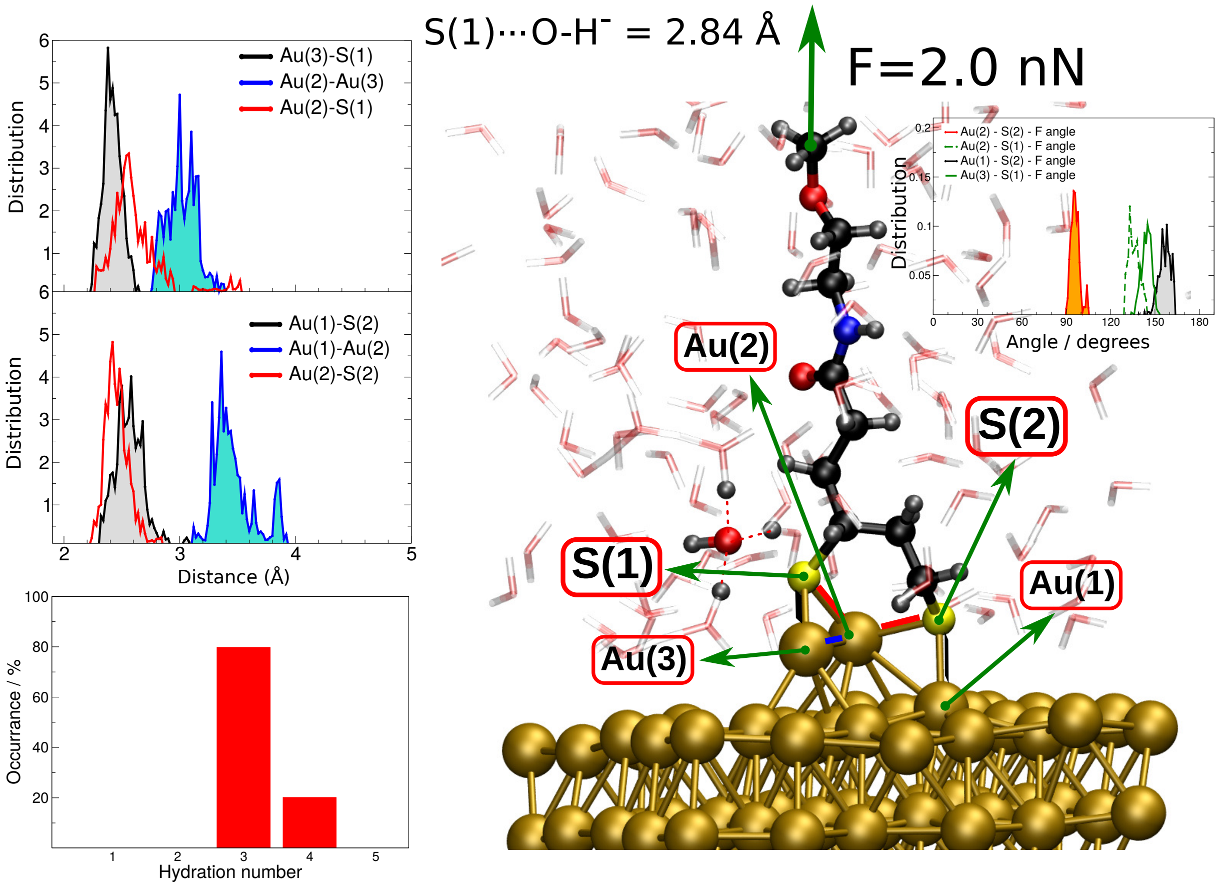

FIG. S28. **Analysis of sulfur S(1)–gold linkage at $F = 2.0$ nN with distance constraint S(1) $\cdots$ OH^{-}=2.84Å.** Right inset: Distribution alignment of gold-sulfur bonds Au(2)-S(2) (orange line), Au(1)-S(2) (gray line), Au(2)-S(1) (dotted green line), and Au(3)-S(1) (green line). Top left panel: Distributions of the bond lengths Au(3)-S(1) (black line), Au(2)-Au(3) (blue line), and Au(2)-S(1) (red line) for the present distance constraint. Middle right panel: Distributions of the bond lengths Au(1)-S(2) (black line), Au(1)-Au(2) (blue line), and Au(2)-S(2) (red line) for the present distance constraint. Bottom right inset: Distribution of hydration numbers of oxygen atom from OH^{-}(aq).

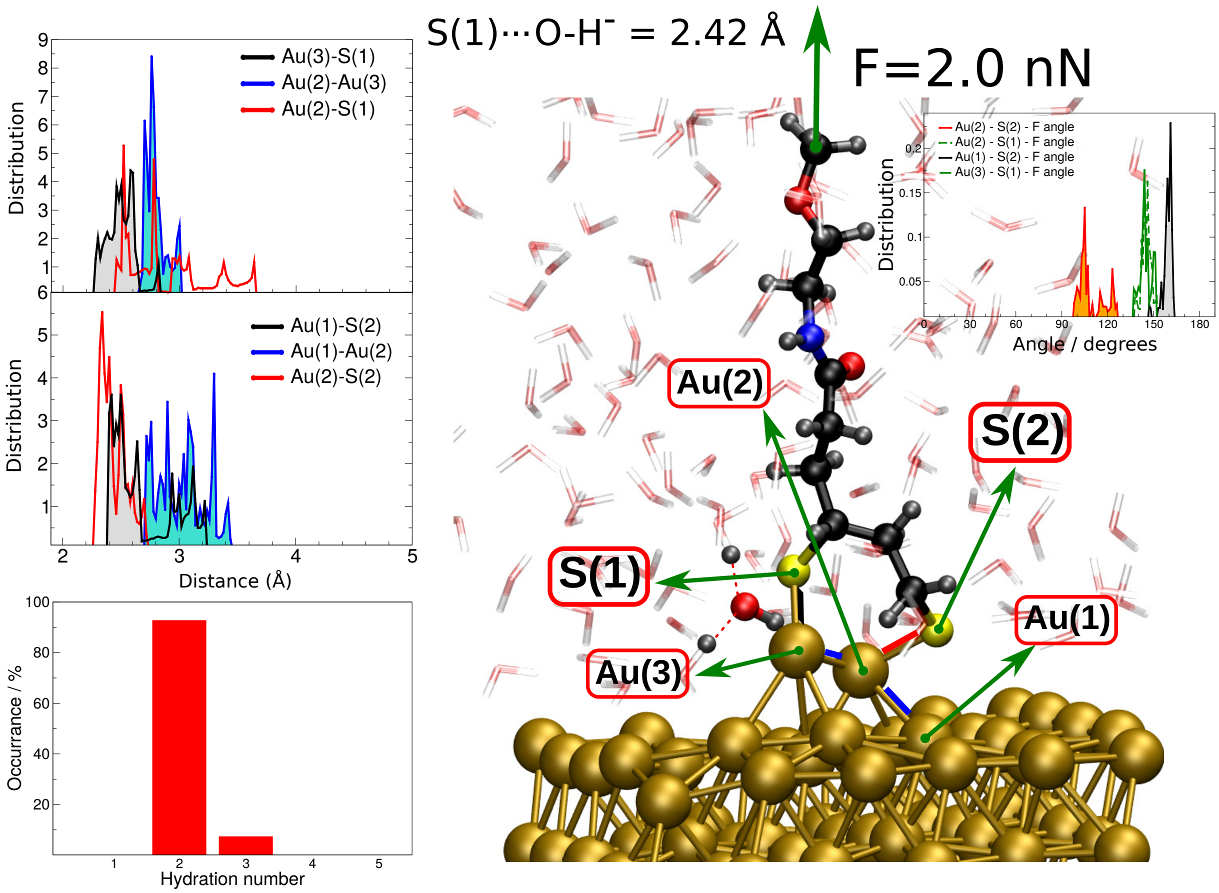

FIG. S29. **Analysis of sulfur S(1)–gold linkage at $F = 2.0$ nN with distance constraint S(1)$\cdots$OH$^-$=2.42Å.** Right inset: Distribution alignment of gold-sulfur bonds Au(2)-S(2) (orange line), Au(1)-S(2) (gray line), Au(2)-S(1) (dotted green line), and Au(3)-S(1) (green line). Top left panel: Distributions of the bond lengths Au(3)-S(1) (black line), Au(2)-Au(3) (blue line), and Au(2)-S(1) (red line) for the present distance constraint. Middle right panel: Distributions of the bond lengths Au(1)-S(2) (black line), Au(1)-Au(2) (blue line), and Au(2)-S(2) (red line) for the present distance constraint. Bottom right inset: Distribution of hydration numbers of oxygen atom from OH$^-$(aq).

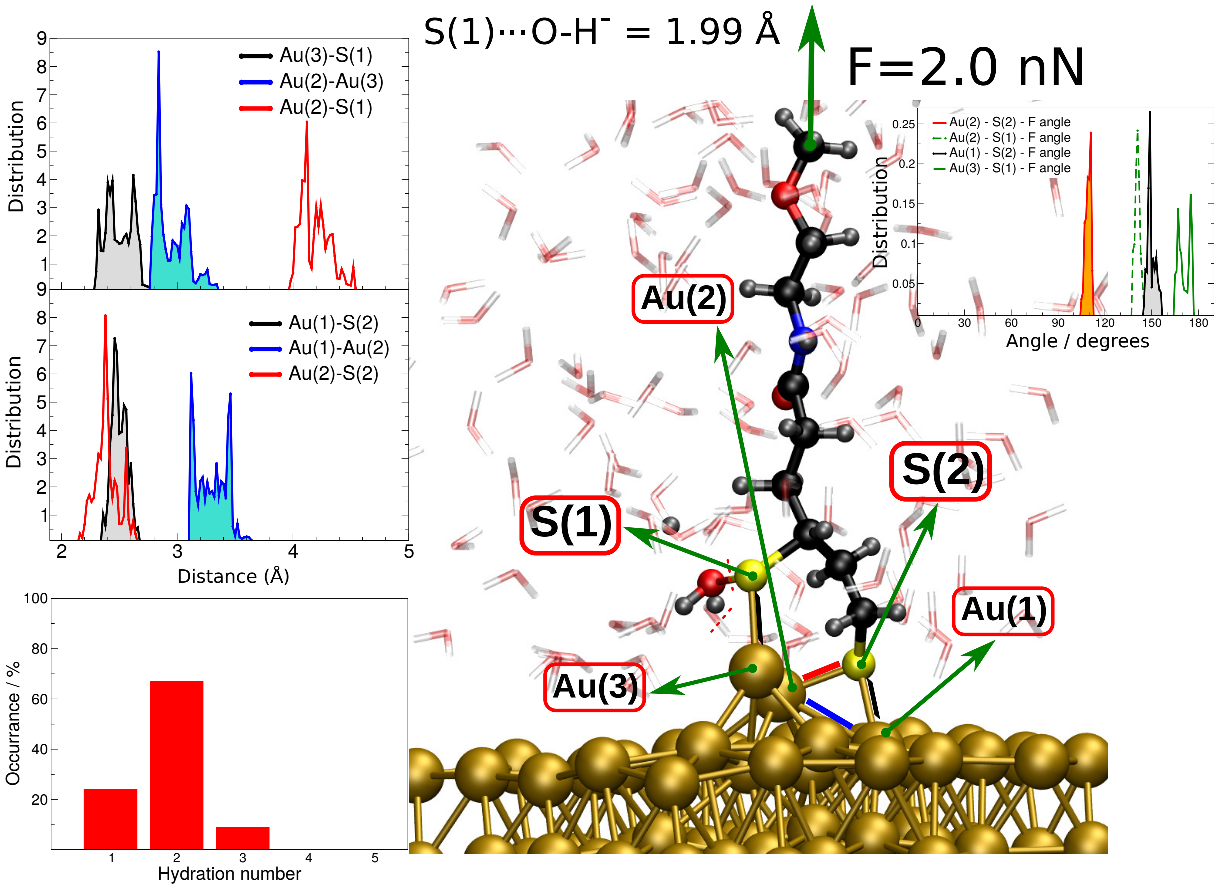

FIG. S30. **Analysis of sulfur S(1)–gold linkage at $F = 2.0$ nN with distance constraint $\mathbf{S(1)\cdots OH^-}$=1.99Å.** Right inset: Distribution alignment of gold-sulfur bonds Au(2)-S(2) (orange line), Au(1)-S(2) (gray line), Au(2)-S(1) (dotted green line), and Au(3)-S(1) (green line). Top left panel: Distributions of the bond lengths Au(3)-S(1) (black line), Au(2)-Au(3) (blue line), and Au(2)-S(1) (red line) for the present distance constraint. Middle right panel: Distributions of the bond lengths Au(1)-S(2) (black line), Au(1)-Au(2) (blue line), and Au(2)-S(2) (red line) for the present distance constraint. Bottom right inset: Distribution of hydration numbers of oxygen atom from OH^-(aq).

C. Reaction Mechanism: Alignment of OH^- and Accessibility of Au–S Bonds for OH^- Attack

In Fig. S31, we analyze the $S\cdots O\text{–}H^-$ angle in the reactant and product state, where collinear alignment would allow for perfect nucleophilic attack of OH^- at sulfur atoms. As it can be seen from Fig. S31, two different pathways were observed for $O\text{–}H^-$ approaching each anchoring sulfur atom: In the first case when S(2) atom is attacked at force $F = 1.2$ nN (top panel in Fig. S31) the $S\cdots O\text{-}H^-$ angle is close to the linear configuration in which the oxygen atom is directly pointing to S(2), and there is still space between $S(2)\cdots O$ so that the oxygen atom from OH^- is coordinated with up to four water molecules. As the $S\cdots OH^-$ distance decreases, i.e. when going from the reactant to product state along the reaction coordinate, there is a slight change of the $S\cdots O\text{–}H^-$ angle to reach a value of around 90–120°. The second scenario is observed for $O\text{–}H^-$ attacking S(1) (see panel for S(1) at force $F = 1.2$ nN in Fig. S31) with the $S\cdots O\text{–}H^-$ angle being around 0–30° in the reactant state – thus now the hydrogen atom from $O\text{–}H^-$ is pointing directly toward S(1), and in this way $O\text{–}H^-$ is nicely coordinated by four water molecules as the oxygen atom is pointing towards the bulk. Afterwards, as the reaction proceeds, the $S\cdots H\text{–}OH^-$ must be broken and, concomitantly, the O atom of OH^- looses some of the hydrating water molecules to reach the final product state.

To check how well each of the four bonds that are important in the breaking event, namely Au(3)–S(1), Au(2)–S(1), Au(2)–S(2) and Au(2)–Au(1), are exposed to the solvent and, thus, also to the attacking OH^- nucleophile, we have introduced in this work an atom–based molecular definition of the spatial accessibility of the active center of the reaction as follows. Each atom X of the PEG–TA molecule is analyzed along the simulated trajectories in such a way that its position is considered and if this atom X is not inside a predefined active space around the specific sulfur atom, that sulfur atom is assigned to be "reactive" since it is not shielded by PEG–TA with respect to solvation by water and putative attack by OH^-. If the opposite is true and some atom X is found to be inside that defined volume, that sulfur atom is considered to be "blocked" with respect to attack and, thus, it cannot be reactive. This so–called "reaction cone" is defined in the spirit of a solvent–accessible volume region in the sense that the $Au\text{–}S\cdots X$ distance does not exceed 4.5 Å and, additionally, the $Au\text{–}S\cdots X$ angle is between 180 and 130° (where X denotes any atom within the PEG–TA

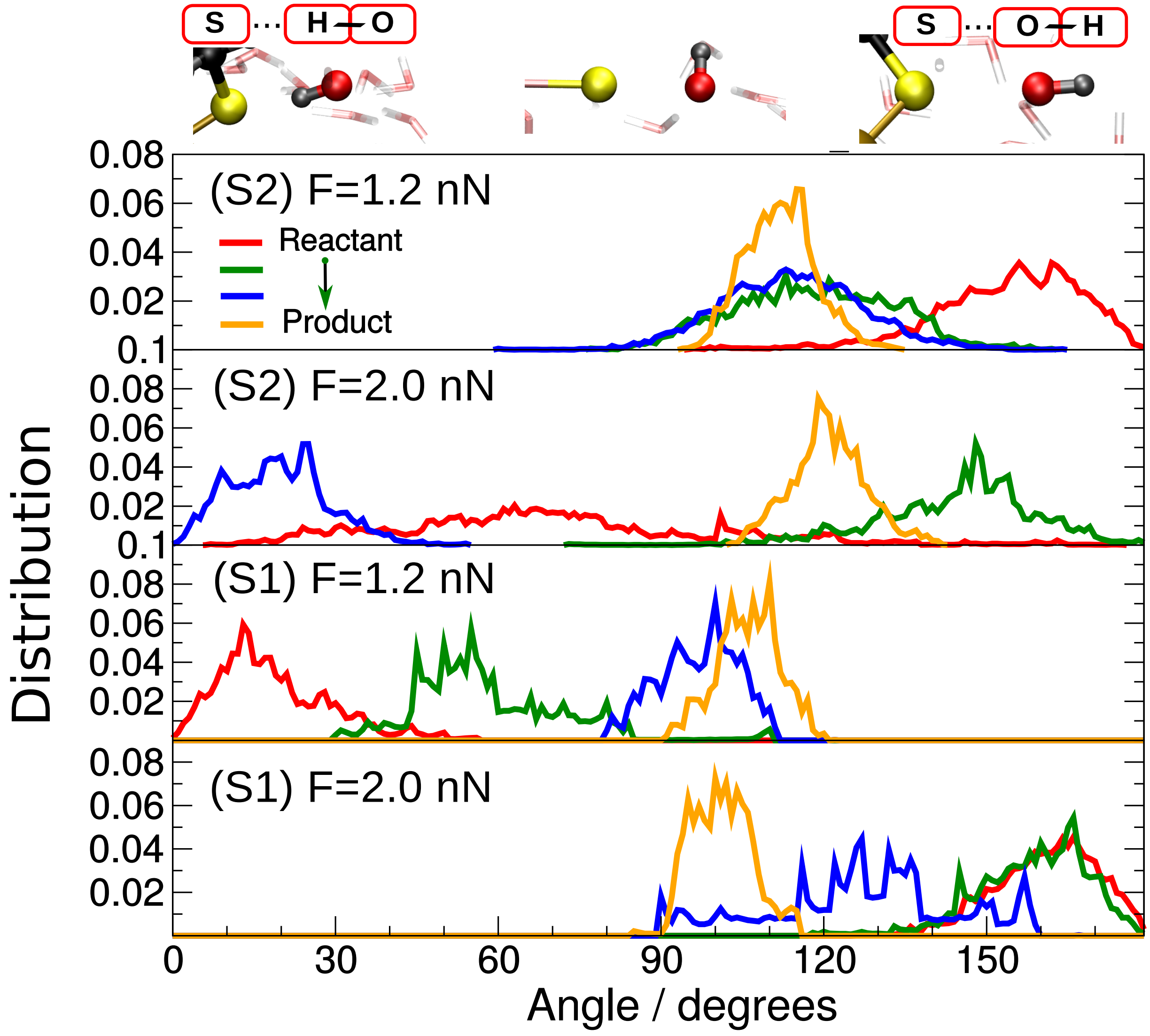

FIG. S31. S···O–H⁻ angle distributions for four selected trajectories along the reaction path at two different forces $F = 1.2$ nN and $F = 2.0$ nN. Distributions from reactant state (red line) to product state (orange line). Top insets show representative situations with S···O-H⁻ angle close to 0° (left inset) and S···O–H⁻ angle around 180° (right inset).

molecule). The results of this detailed analysis are presented in Table 1 of the main text and discussed therein with regard to reactive mechanochemical degradation of PEGylated gold surfaces in alkaline aqueous environments.

---

[1] M. J. Frisch, G. W. Trucks, H. B. Schlegel, G. E. Scuseria, M. A. Robb, J. R. Cheeseman, G. Scalmani, V. Barone, B. Mennucci, G. A. Petersson, H. Nakatsuji, M. Caricato, X. Li, H. P. Hratchian, A. F. Izmaylov, J. Bloino, G. Zheng, J. L. Sonnenberg, M. Hada, M. Ehara, K. Toyota, R. Fukuda, J. Hasegawa, M. Ishida, T. Nakajima, Y. Honda, O. Kitao, H. Nakai, T. Vreven, J. A. Montgomery, Jr., J. E. Peralta, F. Ogliaro, M. Bearpark, J. J. Heyd, E. Brothers, K. N. Kudin, V. N. Staroverov, R. Kobayashi, J. Normand, K. Raghavachari, A. Rendell, J. C. Burant, S. S. Iyengar, J. Tomasi, M. Cossi, N. Rega, J. M. Millam, M. Klene, J. E. Knox, J. B. Cross, V. Bakken, C. Adamo, J. Jaramillo, R. Gomperts, R. E. Stratmann, O. Yazyev, A. J. Austin, R. Cammi, C. Pomelli, J. W. Ochterski, R. L. Martin, K. Morokuma, V. G. Zakrzewski, G. A. Voth, P. Salvador, J. J. Dannenberg, S. Dapprich, A. D. Daniels, Farkas, J. B. Foresman, J. V. Ortiz, J. Cioslowski, and D. J. Fox, "Gaussian09 Revision E.01," Gaussian Inc. Wallingford CT 2009.

[2] D. Marx and J. Hutter, *Ab Initio Molecular Dynamics: Basic Theory and Advanced Methods* (Cambridge University Press, Cambridge, 2009).

[3] J. Lan, V. V. Rybkin, and M. Iannuzzi, J. Phys. Chem. Lett. **11**, 3724 (2020).

[4] P. Maksymovych, D. C. Sorescu, and J. T. Yates, Phys. Rev. Lett. **97**, 146103 (2006).

[5] P. Giannozzi, S. Baroni, N. Bonini, M. Calandra, R. Car, C. Cavazzoni, D. Ceresoli, G. L. Chiarotti, M. Cococcioni, I. Dabo, A. D. Corso, S. d. Gironcoli, S. Fabris, G. Fratesi, R. Gebauer, U. Gerstmann, C. Gougoussis, A. Kokalj, M. Lazzeri, L. Martin-Samos, N. Marzari, F. Mauri, R. Mazzarello, S. Paolini, A. Pasquarello, L. Paulatto, C. Sbraccia, S. Scandolo, G. Sclauzero, A. P. Seitsonen, A. Smogunov, P. Umari, and R. M. Wentzcovitch, J. Phys.: Condens. Matter **21**, 395502 (2009).

[6] J. P. Perdew, K. Burke, and M. Ernzerhof, Phys. Rev. Lett. **77**, 3865 (1996).

[7] D. Vanderbilt, Phys. Rev. B **41**, 7892 (1990).

[8] M. E. Zoloff Michoff, J. Ribas-Arino, and D. Marx, Phys. Rev. Lett. **114**, 075501 (2015).

[9] M. E. Zoloff Michoff, J. Ribas-Arino, and D. Marx, Phys. Rev. Lett. **122**, 086801 (2019).

[10] J. Ribas-Arino and D. Marx, Chem. Rev. **112**, 5412 (2012).

[11] M. K. Beyer, Angew. Chem. Int. Ed. **42**, 4913 (2003).

[12] F. Xia, A. K. Bronowska, S. Cheng, and F. Gräter, J. Phys. Chem. B **115**, 10126 (2011).

[13] D. Van Der Spoel, E. Lindahl, B. Hess, G. Groenhof, A. E. Mark, and H. J. C. Berendsen, J. Comput. Chem. **26**, 1701 (2005).

[14] W. Jorgensen, D. Maxwell, and J. Tirado-Rives, J. Am. Chem. Soc. **118**, 11225 (1996).

[15] J. Hutter and *et al.*, "`CPMD` Program Package," See `http://www.cpmd.org`.

[16] S. Grimme, J. Antony, S. Ehrlich, and H. Krieg, J. Chem. Phys. **132**, 154104 (2010).

[17] D. Muñoz-Santiburcio and D. Marx, Phys. Rev. Lett. **119**, 056002 (2017).

[18] D. Muñoz-Santiburcio and D. Marx, Chem. Sci. **8**, 3444 (2017).

[19] J. Daru, H. Forbert, J. Behler, and D. Marx, Phys. Rev. Lett. **129**, 226001 (2022).

[20] N. Stolte, J. Daru, H. Forbert, J. Behler, and D. Marx, J. Phys. Chem. Lett. **15**, 12144 (2024), pMID: 39607891.

[21] J. Blumberger, B. Ensing, and M. L. Klein, Angew. Chem. Int. Ed. **118**, 2959 (2006).

[22] D. Marx, A. Chandra, and M. E. Tuckerman, Chem. Rev. **110**, 2174 (2010).

[23] A. Vargas, G. Santarossa, M. Iannuzzi, and A. Baiker, Phys. Rev. B **80**, 195421 (2009).

[24] M. Gao, A. Lyalin, M. Takagi, S. Maeda, and T. Taketsugu, Journal of Physical Chemistry C **119**, 11120.